Space Sci Rev (2009) 145: 137–191
DOI 10.1007/s11214-009-9508-7

Advances in Plasmaspheric Wave Research with CLUSTER and IMAGE Observations

Arnaud Masson · Ondrej Santolík · Donald L. Carpenter · Fabien Darrouzet · Pierrette M. E. Décréau · Farida El-Lemdani Mazouz · James L. Green · Sandrine Grimald · Mark B. Moldwin · František Němec · Vikas S. Sonwalkar

Received: 13 October 2008 / Accepted: 8 April 2009 / Published online: 29 May 2009
© Springer Science+Business Media B.V. 2009

Abstract This paper highlights significant advances in plasmaspheric wave research with CLUSTER and IMAGE observations. This leap forward was made possible thanks to the new observational capabilities of these space missions. On one hand, the multipoint view of the four CLUSTER satellites, a unique capability, has enabled the estimation of wave characteristics impossible to derive from single spacecraft measurements. On the other hand, the IMAGE experiments have enabled to relate large-scale plasmaspheric density structures with

A. Masson (✉)
Science Operations Department, ESA/ESTEC, Keplerlaan 1, 2201-AZ Noordwijk, The Netherlands
e-mail: Arnaud.Masson@esa.int

O. Santolík · F. Němec
Faculty of Mathematics and Physics, Institute of Atmospheric Physics, Charles University, Praha, Czech Republic

O. Santolík
e-mail: ondrej.santolik@mff.cuni.cz

F. Němec
e-mail: frantisek.nemec@mff.cuni.cz

D.L. Carpenter
Space, Telecommunications and Radioscience Laboratory (STAR), Stanford University, Stanford, CA, USA
e-mail: dlc@nova.stanford.edu

F. Darrouzet
Belgian Institute for Space Aeronomy (BIRA-IASB), Brussels, Belgium
e-mail: Fabien.Darrouzet@oma.be

P.M.E. Décréau · F. El-Lemdani Mazouz
Laboratoire de Physique et Chimie de l'Environnement et de l'Espace (LPC2E), CNRS/Université d'Orléans, Orléans, France

P.M.E. Décréau
e-mail: Pierrette.Decreau@cnrs-orleans.fr

F. El-Lemdani Mazouz
e-mail: mazouz@cnrs-orleans.fr

wave observations and provide radio soundings of the plasmasphere with unprecedented details. After a brief introduction on CLUSTER and IMAGE wave instrumentation, a series of sections, each dedicated to a specific type of plasmaspheric wave, put into context the recent advances obtained by these two revolutionary missions.

Keywords Plasmasphere · CLUSTER · IMAGE · Waves

1 Introduction

Plasma waves play a fundamental role in our geospace environment. In particular, they are key to understand the way mass and energy are transfered from the magnetotail to the plasmasphere, the ionosphere and finally the atmosphere. Particles propagating in the magnetosphere indeed lose or gain energy via wave–particle interactions while waves are amplified or damped. Particles can also be diffused into the loss cone and precipitate to lower altitudes. But how much each type of wave contributes to this process and under which geophysical conditions? In order to answer this difficult question, a complete overview on plasma waves is needed to understand how and under which conditions waves are generated and how they propagate from their source regions.

A key region where such waves are generated is the plasmasphere, either within it or in its near vicinity. Various waves are found in this region from a few mHz to a few MHz, either electrostatic or electromagnetic. Ground-based observatories and space missions since the 1950s have collected a wealth of information about them (e.g., Lemaire and Gringauz 1998, p. 94) but many questions remained open before the launch of the European Space Agency (ESA) CLUSTER and the NASA IMAGE space missions in 2000. A review of whistler-mode type waves observed within the plasmasphere by IMAGE and DE-1 spacecraft can be found in Green and Fung (2005) and Green et al. (2005b).

This paper highlights recent advances obtained by the CLUSTER and the IMAGE missions on plasmaspheric wave phenomena in the medium frequency (MF) range (300 kHz–3 MHz) down to the very low frequency (VLF) range (3–30 kHz), the ultra low frequency (ULF) range (300 Hz–3 kHz) and the extremely low frequency (ELF) range (3–30 Hz). Both missions can be seen as a step forward in our understanding of these phenomena. On one hand, the multipoint view of the four CLUSTER satellites, a unique capability, has enabled the estimation of wave characteristics impossible to derive from single spacecraft measurements.

J.L. Green
NASA Headquarters, Washington, DC, USA
e-mail: James.L.Green@nasa.gov

S. Grimald
Mullard Space Science Laboratory (MSSL), Dorking, UK
e-mail: sg2@mssl.ucl.ac.uk

M.B. Moldwin
Institute of Geophysics and Planetary Physics (IGPP), University of California, Los Angeles, CA, USA
e-mail: mmoldwin@igpp.ucla.edu

V.S. Sonwalkar
Department of Electrical and Computer Engineering, University of Alaska Fairbanks, Fairbanks, AK, USA
e-mail: ffvss@uaf.edu

This includes the first quantitative estimation in three dimensions of the size of wave source regions (Sect. 8), their localizations and beaming properties by triangulation (Sect. 4). On the other hand, IMAGE was the first mission dedicated to remotely study the plasmasphere. The Radio Plasma Imager (RPI) onboard IMAGE was the first radio sounder launched above the plasmasphere enabling the discovery of new wave echoes, the remote derivation of density profiles and the study of field-aligned irregularities in the plasmasphere with unprecedented details (Sects. 5, 6, 7 and 11). Together with RPI, the IMAGE spacecraft carried several imagers including an Extreme UltraViolet (EUV) imager able to capture, for the first time, the entire plasmasphere—distribution of helium ions—in a single shot, every 10 minutes. Thus, EUV enabled for the first time to monitor changes in the plasma distribution of the overall plasmasphere and the size and evolution of large-scale plasmaspheric structures such as notches and plumes. As described in Sect. 3, plasmaspheric notches observed by EUV have been studied with wave measurements made by GEOTAIL to learn more about the source of kilometric continuum. Similarly, CLUSTER data have been combined with observations from the DOUBLE STAR equatorial spacecraft TC-1, which routinely detected chorus emissions, as well as the low altitude DEMETER spacecraft. Recent advances on plasmaspheric hiss have also benefited from measurements of the DE-1 and CRRES satellites (Sect. 9).

This review is the result of a collective effort, gathering the contributions of several scientists. A brief introduction to the CLUSTER and IMAGE instruments related to plasmaspheric wave phenomena is given in Sect. 2 (see also De Keyser et al. 2009, this issue). Then a series of nine sections describes the advances obtained on six waves and three types of sounding echoes. These sections are organized by decreasing frequency of the waves/echoes. Section 3 is dedicated to IMAGE and GEOTAIL observations of kilometric continuum (KC), the high-frequency range of a more general wave phenomenon called non-thermal continuum (NTC). Advances on NTC at lower frequency observed with CLUSTER are detailed in Sect. 4. The next three sections describe what has been learned so far from Z-mode (Sect. 5), whistler-mode (Sect. 6) and proton cyclotron echoes (Sect. 7) received by the RPI instrument. The following three sections are dedicated to VLF and ELF waves impacting the relativistic electron content of the radiation belts, namely: chorus (Sect. 8), plasmaspheric and mid-latitude hisses (Sect. 9), equatorial noise (Sect. 10). The last section (Sect. 11) deals with the determination of the average ion mass in the plasmasphere using ground-based ULF wave diagnostics and electron density profiles derived from RPI soundings. It is worth noting that the locations of the source regions of most of these waves are strongly linked with the position of the plasmapause, itself strongly influenced by large-scale electric fields (Matsui et al. 2009, this issue).

A set of acronyms is used throughout this paper. The Earth radius will be referred as R_E, the magnetic local time as MLT and the magnetic latitude as *MLAT*. The localisation of wave phenomena in the plasmasphere are often expressed in terms of L-shell (McIlwain 1961). For example, "$L = 4$" describes the set of the Earth's magnetic field lines, which cross the magnetic equator at 4 R_E from the center of the Earth. The plasmasphere boundary layer introduced by Carpenter and Lemaire (2004) is often abbreviated as PBL. The acronyms of the main plasma frequencies used in this paper are the following: f_{pe} for the electron plasma frequency, f_{ce} for the electron cyclotron frequency also called electron gyrofrequency, f_{uh} and f_{lh} for the upper and lower hybrid frequencies. Finally, the acronyms of the CLUSTER satellites are C1, C2, C3 and C4, conventionally color-coded as black, red, green and magenta respectively.

2 CLUSTER and IMAGE Wave Instrumentation

2.1 CLUSTER Wave Instruments

The four CLUSTER satellites carry eleven identical instruments to measure the electric field, the magnetic field and the electron and ion distribution functions (Escoubet et al. 1997). Three of them are particularly suited to study wave phenomena within or in the vicinity of the plasmasphere (see Sects. 4, 8, 9 and 10):

- The Spatio-Temporal Analysis of Field Fluctuations (STAFF) instrument measures the magnetic field between 8 Hz and 4 kHz with a three axis search coil magnetometer. Its spectrum analyzer performs auto- and cross-correlations between the three magnetic components estimated by the search coil and the two electric components measured by the Electric Field and Wave (EFW) experiment (Gustafsson et al. 2001). From auto-correlations, the energy densities of electric and magnetic components are inferred, together with the electrostatic/electromagnetic nature of the observed waves. The cross-power spectra are needed to estimate the polarization characteristics of electromagnetic waves. The time resolution varies between 0.125 s and 4 s. For a complete description of STAFF, see Cornilleau-Wehrlin et al. (2003).
- At higher frequencies (2–80 kHz), radio wave signals are continuously monitored by the active soundings and passive measurements of the Waves of HIgh frequency and Sounder for Probing of Electron density by Relaxation (WHISPER) instrument. The hardware of WHISPER mainly consists of a pulse transmitter, a wave receiver and a wave spectrum analyzer. Electric signals are acquired by the EFW electric antennas and only the onboard calculated fast fourier transform of the digital electric waveforms acquired are transmitted to the ground. A passive spectrum is recorded every 2.2 s and an active one every 52 s in normal mode for a frequency resolution of 162 Hz. Unlike a passive receiver, such a relaxation sounder enables to trigger plasma resonances when the medium does not show them naturally. For a detailed description of WHISPER, see Décréau et al. (2001).
- The Wide-Band Data (WBD) experiment consists of a wide-band passive receiver, which provides electric waveforms with high time resolution in three possible frequency bands: 100 Hz to 9.5 kHz, 100 Hz to 19 kHz and 700 Hz to 77 kHz. The first frequency band is the one mostly operated to study plasmaspheric wave phenomena. It provides continuous waveforms with a 27.4 kHz sampling rate. When no soundings are performed, WBD electric data may be seen as high resolution zooms of WHISPER spectra. For a complete description of WBD, see Gurnett et al. (2001).

2.2 IMAGE Wave Related Phenomena Instruments

IMAGE (Imager for Magnetopause to Aurora Global Exploration) was the first satellite dedicated to imaging the Earth's inner magnetosphere (Burch 2000). It was equipped with six instruments, which use neutral atom, ultraviolet and radio imaging techniques. Two of these instruments have been particularly used to study wave phenomena in the plasmasphere (see Sects. 3, 5, 6, 7 and 11):

- The Extreme UltraViolet (EUV) imager was able to picture the entire plasmasphere in a single "snapshot". It captured the helium ion (He^+) distribution outside Earth's shadow by measuring their emission line at 30.4 nm. He^+ is the second most abundant ion species in the plasmasphere accounting for roughly 20% of the plasma population while hydrogen ion (H^+), the most abundant one, has no optical emission. Because the plasmaspheric

He^+ emission is optically thin, the integrated column density of He^+ along the line-of-sight through the plasmasphere is directly proportional to the intensity of the emission. Moreover, the 30.4 nm emission line is the brightest ion emission from the plasmasphere and is spectrally isolated with a negligible background. For a full description of EUV, see Sandel et al. (2000).

– The Radio Plasma Imager (RPI) was a low-power radar with three dipole antennas. The two spin plane antennas were of lengths 370 m and 470 m tip-to-tip (Benson et al. 2003) while the one along the spin axis was 20 m long (spin rate: 0.5 rpm). The spin plane antennae are so far the longest ever deployed in space for such an instrument. RPI was able to locate regions of various plasma densities by observing radar echoes from the plasma. These echoes were reflected when the radio frequency was equal to the plasma frequency. By stepping the transmitted signal frequency through a wide frequency range (3 kHz–3 MHz), features of various plasma densities were observed. Derived densities, from those locations returning radio sounding echoes, were combined with line-of-sight images captured by EUV to infer quantitative, global distributions of plasmaspheric plasma. For a full description of RPI, see Reinisch et al. (2000).

3 Kilometric Continuum

3.1 Previous Observations

Low frequency non-thermal continuum radiation has been observed extending from ∼15 kHz to as high as ∼300 kHz although it is rarely observed above ∼90 kHz. However, Hashimoto et al. (1999) discovered a type of high frequency continuum radiation that is observed in the 100–800 kHz frequency range and as such, will escape the magnetosphere once it has been generated. These authors named this emission kilometric continuum (KC) due to the fact that the emission closely resembles the discrete emission band structure of the lower frequency non-thermal continuum in frequency–time spectrograms, has many other similar characteristics, and is probably generated by the same mechanism. It is important to note that KC is always observed without an accompanying lower frequency trapped component. The discovery of this high frequency KC emission has sparked considerable interest in further understanding various aspects of this radiation, what makes it different from its lower frequency counterpart, and the relationship with the plasmasphere and the plasmapause.

The spectrogram on Fig. 1 clearly shows the discrete emissions bands of KC extending from 17:00 to 24:00 UT. The frequency range for KC is approximately the frequency range of auroral kilometric radiation (AKR), but as shown in Fig. 1, there are significant differences that can be used to easily distinguish between these two emissions. KC has a narrow band structure over a number of discrete frequencies with time while AKR is observed to be a broader band emission with emissions extending over a large frequency range sporadically

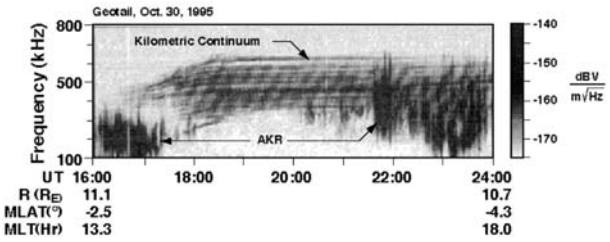

Fig. 1 A frequency–time spectrogram of KC emissions measured on 30 October 1995 by the Plasma Wave Instrument (PWI) onboard GEOTAIL. (Adapted from Hashimoto et al. 1999)

and can be seen from 16:00 to 17:00 UT and from 21:30 to 24:00 UT in that spectrogram. In order to determine the source of the KC emission Hashimoto et al. (1999) performed direction finding using spin modulation of the emission. The resulting directions (shown in Fig. 4) with time, as correlated with the spectrogram data, indicated that the emission was generated from a very broad source region of the plasmasphere. Due to the high emission frequency of KC and its lack of correlation with geomagnetic activity, the source of KC was originally believed to lie deep within the plasmasphere (Hashimoto et al. 1999). Soon after these results were published, Carpenter et al. (2000) suggested that the source region for KC was coming from plasmaspheric cavities deep within the plasmasphere. From their analysis of over 1764 near-equatorial electron density profiles from CRRES, deep density troughs or cavities were observed on ∼13% of the passes (Carpenter et al. 2000).

3.2 IMAGE Observations

It would take new observations of the plasmasphere from the EUV and RPI instruments onboard IMAGE along with simultaneous observations of KC from the Plasma Wave Instrument (PWI) onboard GEOTAIL to understand what plasmaspheric structures are the source region of KC thereby reaching a new understanding of plasmaspheric structure and dynamics. From the perspective of the CRRES observations the results of Carpenter et al. (2000) are compelling and appear to establish cavity-like structures in the plasmasphere. The IMAGE observations show them as plasmaspheric notches, which are the primary sources of KC.

Figure 2 illustrates that the location of the KC source region within a plasmaspheric notch, and the resulting emission cone pattern of the radiation, as shown from ray tracing calculations, is consistent with many of the previous observations. Figure 2a is a frequency–time spectrogram (passive mode) from PWI onboard GEOTAIL showing the banded structure of KC. The slanted vertical emissions are all Type III solar radio bursts. Figure 2b shows the magnetic longitude versus the equatorial radial distance of the plasmapause (derived from the right insert of the EUV image of the plasmasphere) and the GEOTAIL position during the KC observations of panel (**a**). As observed by EUV, plasmaspheric notch are large "bite-outs" in the plasmasphere in which plasma has largely been evacuated from a nominal plasmapause to somewhere deep within the plasmasphere (see also Darrouzet et al. 2009, this issue). This structure is significantly different than a density cavity of some size and depth within the plasmasphere. Figure 2b, left insert, presents a ray tracing analysis showing that the structure of the plasmaspheric notch has a significant effect on the shape of the resulting emission cone through refraction of the radiation generated from a small source region located at the magnetic equator deep within the plasmaspheric notch. The correspondence of KC observations with plasmaspheric notches, as shown in Fig. 2, is not an isolated instance. Green et al. (2004) found from a year's worth of observations of GEOTAIL KC measurements and EUV images of plasmaspheric notches that the vast majority (94%) of the 87 cases studied showed this correspondence. Their results also showed that a density depletion or notch structure in the plasmasphere is typically a critical condition for the generation of KC but that the notch structures do not always provide the conditions necessary for the generation of the emission.

If KC source regions were located deep within a plasmaspheric notch, they can be used to further study the properties of the KC emission cone and the depth of notches. From a statistical analysis Fig. 3a shows the number of occurrences of KC observed by PWI onboard GEOTAIL, associated with plasmaspheric notches observed by EUV onboard IMAGE, with the magnetic longitudinal extent of the emission. This analysis assumed that the plasmaspheric notches were corotating with the plasmasphere. From these events the median in the

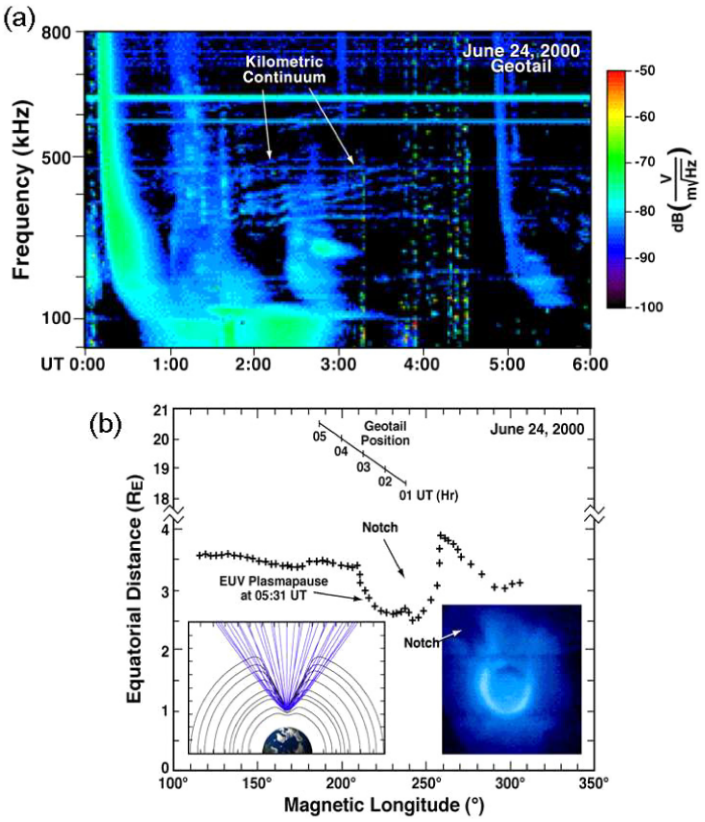

Fig. 2 (**a**) Kilometric continuum observations from PWI onboard GEOTAIL on 24 June 2000 from 00:00 to 06:00 UT. (**b**) The location of GEOTAIL during the KC observations and the extracted location of the plasmapause from IMAGE/EUV data are plotted in magnetic longitude versus equatorial distance. Inserted into panel (**b**) are model ray tracing calculations (*left*) and the EUV image data (*right*). (Adapted from Green et al. 2002, 2004)

longitudinal extent of the KC emission cone is ∼44°. Assuming an average plasmaspheric model and that KC is generated near the upper hybrid frequency an estimation of the depth of notch structures can be determined. Figure 3b shows the number of occurrences of the highest frequency source of the same KC events versus equatorial radial distance as an estimation of the deepest location of the KC source region. The distribution has a large peak with the median and the mean of the distribution at approximately the same equatorial radial distance of 2.4 R_E.

Observations of the plasmasphere and KC emissions from the IMAGE instruments provide a new perspective in which previous CRRES and GEOTAIL measurements can be interpreted self-consistently to obtain additional insights into plasmaspheric dynamics and structure. Figure 4a shows the direction finding measurements of Hashimoto et al. (1999) indicating an extensive emission region for KC. Figures 4b–f illustrate how a small source region of KC deep within in a plasmaspheric notch can generate an emission cone that is also consistent with the direction finding measurements. The proposed plasmaspheric notch and the corresponding KC emission cone all corotate with the plasmasphere and are shown over the same 12-hour period. GEOTAIL was in the proposed emission cone and ob-

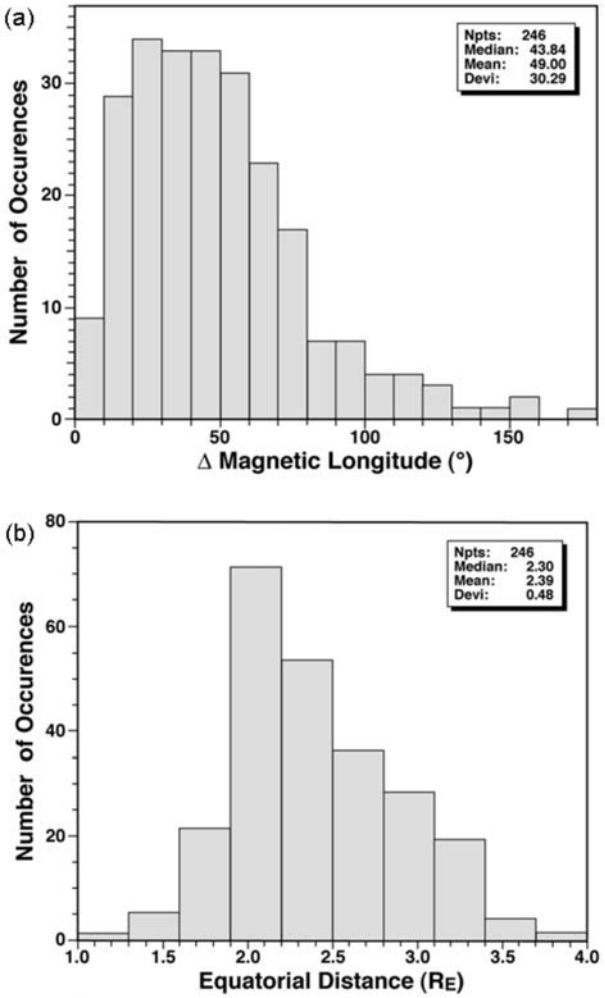

Fig. 3 (**a**) Number of occurrences of KC (observed by PWI onboard GEOTAIL) associated with plasmaspheric notches (observed by EUV onboard IMAGE) with the magnetic longitudinal extent of the emission. (**b**) Number of occurrences of the highest frequency source of the same KC events versus equatorial radial distance as an estimation of the deepest location of the KC source

served KC radiation starting at approximately 16:00 UT until 04:00 UT of the next day. During this time, the corotating plasmasphere sweeps the emission cone across and finally past the GEOTAIL spacecraft in a way completely consistent with the direction finding results.

Carpenter et al. (2000) reported significant density variations or cavities in the plasmasphere in which KC at many times were observed. The obvious confinement of KC to a cavity-like structure led those authors to propose that the radiation would be trapped in plasmaspheric cavities at frequencies below the density of the outer cavity wall. With the advent of the IMAGE mission a new interpretation has arisen to these observations as presented by Green et al. (2002). Figure 5a assumes a notch structure, like those that have been observed by EUV, would exist at the time of the CRRES observations (1990–1991). What is also shown is a typical CRRES orbit plotted in the same magnetic longitude and L coordinates. By using magnetic longitude and L coordinates the orbit of CRRES is then presented in the same reference frame as a corotating plasmasphere and notch structure. Figure 5b approxi-

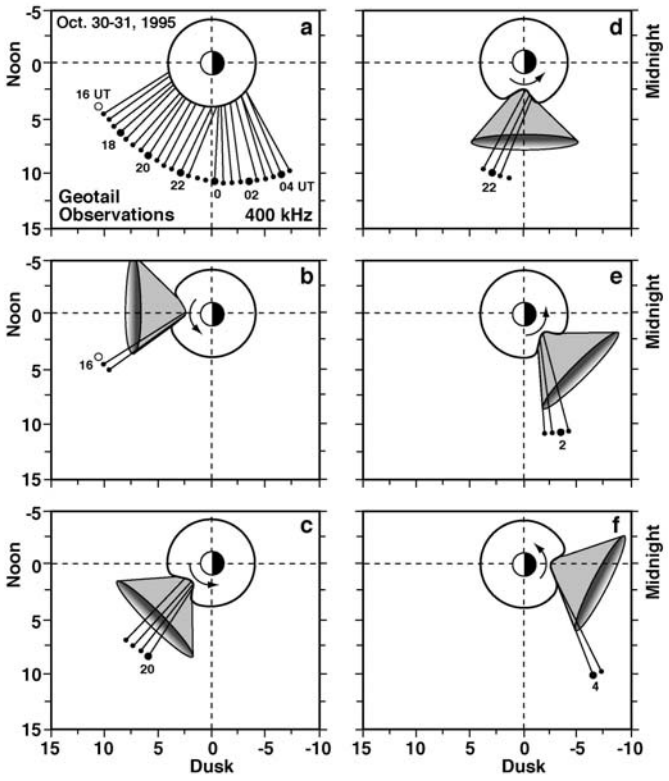

Fig. 4 Direction finding measurement (**a**) from Hashimoto et al. (1999) of KC at 400 kHz are reinterpreted as being completely consistent with respect to the source of KC emitted from a corotating plasmaspheric notch (**b**)–(**f**). (Adapted from Green et al. 2002)

mates the corresponding density structure that would be observed. The resulting qualitative density structure of the plasmaspheric notch, shown in Fig. 5b, is indistinguishable from the density cavities structures reported by Carpenter et al. (2000) and delineated as the upper hybrid resonance emissions. The CRRES observations of the confinement of KC to plasmaspheric cavities, reported by Carpenter et al. (2000) can then alternately be interpreted as KC radiation generated at the plasmapause, at the base of a plasmaspheric notch. Refraction near the source region of the steep density wall of the cavity would then confine the emission to within the notch structure as the ray tracing calculations have shown.

3.3 Conclusions

In summary, recent observations of KC from IMAGE and GEOTAIL have provided a new opportunity to understand plasmaspheric structures and dynamics. KC is always observed without an accompanying lower frequency trapped non-thermal continuum component but is almost certainly generated by the same emission mechanism. Plasmaspheric notches, reported earlier as deep plasmaspheric density cavities, are the source of KC. Much like the lower frequency non-thermal continuum emissions generated at the plasmapause, it is now well established that KC is generated at the newly established plasmapause, deep within a notch structure, near the magnetic equator. From the KC observations, plasmaspheric

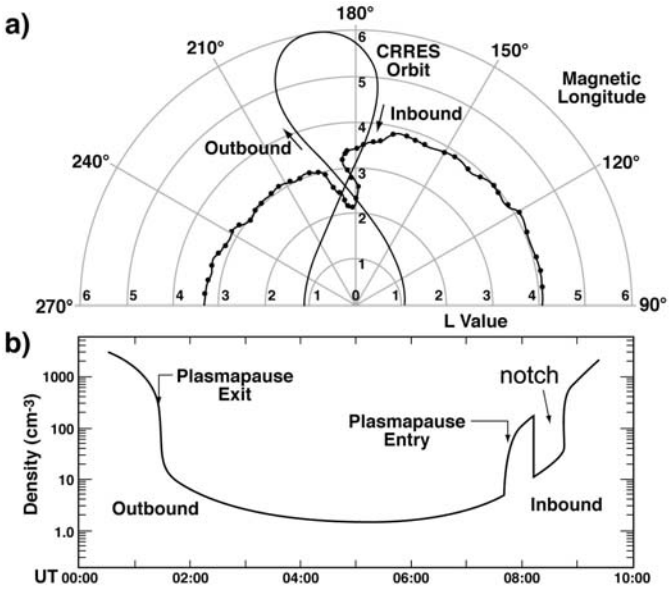

Fig. 5 (**a**) A typical orbit of the CRRES spacecraft in magnetic longitude and L value plotted over a typical plasmaspheric notch. (**b**) Approximate variation in density that would be observed assuming that a notch structure like this would exist at the time of CRRES

notches are typically as deep as $\sim 2\ R_E$ but can be deeper within the plasmasphere. The average beam width of KC has been found to be $\sim 44°$. The confinement of the KC emission cone, as shown by the ray tracing calculations, due to the steep densities of the walls of the notch structure therefore indicates that the average size of plasmaspheric notches must also be $\sim 44°$ in longitude. Due to the strong relationship between KC and plasmaspheric notches, the long term set of observations of KC by GEOTAIL, extending more than 10 years could now be use to make long-term studies that relate to plasmaspheric notch structure and dynamics.

There are a number of outstanding questions that need to be addressed concerning the generation and propagation of the KC emissions such as:

- Is the motion of the plasmapause inwards coupled with a sufficiently large density gradient necessary and sufficient for the generation of KC? Is the free energy source necessary for the creation of electrostatic waves that are precursors to KC always present, or is the free energy source dependent on the state of the magnetosphere?
- KC often exhibits a banded frequency structure consistent with $(n + \frac{1}{2}) f_{ce}$ source, but frequently the structure appears more complex. Can density ducts near the plasmapause explain the more complex structure or do other mechanisms need to be investigated like dynamic motion of the plasmasphere boundary layer?
- For highly disturbed times large changes occur in the inner magnetosphere magnetic field intensity. Can this change be detected remotely in the spectral band spacing of escaping KC? Can the analysis of the frequency structure of escaping KC indicate the state of the plasmasphere and the inner magnetosphere magnetic field?

4 Non-Thermal Continuum

4.1 CLUSTER Observations

4.1.1 Assets of the CLUSTER Mission

The WHISPER instrument measures electric field in a frequency range (2–80 kHz) well adapted to study non-thermal continuum (NTC) waves, both in the trapped frequency band (∼1–20 kHz) and in the lowest part of the escaping frequency band (∼20–200 kHz). The WBD instrument completes the view by providing high resolution snapshots and wave forms on a similar frequency range (0–77 kHz) when studying NTC waves. The major assets of the CLUSTER observatory about NTC studies are four fold.

- *Orbital characteristics.* The satellites travel from southern to northern hemisphere and cross or skim the plasmasphere around perigee at radial geocentric distances of ∼4.3 R_E. Such orbit configurations provide excellent view points on the radio beams directly emitted at close distances, from equatorial plasmapause sources, when those are placed inward from the orbit, i.e., when the plasmasphere is sufficiently contracted. The polar orbit of CLUSTER near its perigee is comparable to that of DE-1 near its apogee, of geocentric distance ∼4.5 R_E. CLUSTER platforms spin under different conditions than DE-1: Spin axis are normal to XY GSE (geocentric solar ecliptic) plane in CLUSTER case, whereas DE-1 spins in a cartwheel manner with the spin axis parallel to XY GSE plane. CLUSTER offers thus complementary views to those obtained by DE-1 in the past. As a consequence, typical DE-1 observations of NTC beaming properties can be reinterpreted in view of CLUSTER observations, in a similar manner IMAGE views help interpreting CRRES past observations of KC. Away from perigee, CLUSTER offers views at large distances from sources. The electric field measured there results often from a superposition of waves emitted from various and multiple sources. Detailed directivity estimations, made possible thanks to good frequency and time resolutions, help to distinguish each of the main source regions from the others.
- *Instrument performances.* A good time resolution (electric field spectra delivered at a rate of ∼2 s) allows directivity measurements in 2-D (direction of the wave vector in the spin plane) at successive positions on the orbit (∼300 km apart).
- *Multipoint observations.* Performances of the constellation vary according to spacecraft separation, which is varied along the mission phase. The spatio-temporal analysis of beam properties is made possible by comparing observations over small time intervals and small distances in space, i.e., during mission phases at small or medium separation (100 to 1000 km). In addition, compared wave vector directions lead to source localization. This can be done via triangulation, either from several spacecraft illuminated by the same beam at the same time (during mission phases at large separation), or from a single drifting spacecraft viewpoint, after stability of the beam has been assessed from compared observations.
- *Plasma diagnostic from a relaxation sounder.* In addition to spectral and geometric analysis of radiated beams, CLUSTER offers the possibility of analyzing intense electrostatic waves, which are potential sources of non-thermal radiations.

This section focuses on observations of NTC radiations (excluding trapped continuum signatures) when CLUSTER is either in the outer plasmasphere or in the polar cap region. The tetrahedron shape achieved at large geocentric distances turns to an elongated shape near perigee. Figure 6a displays the near Earth magnetic field configuration and the orbit

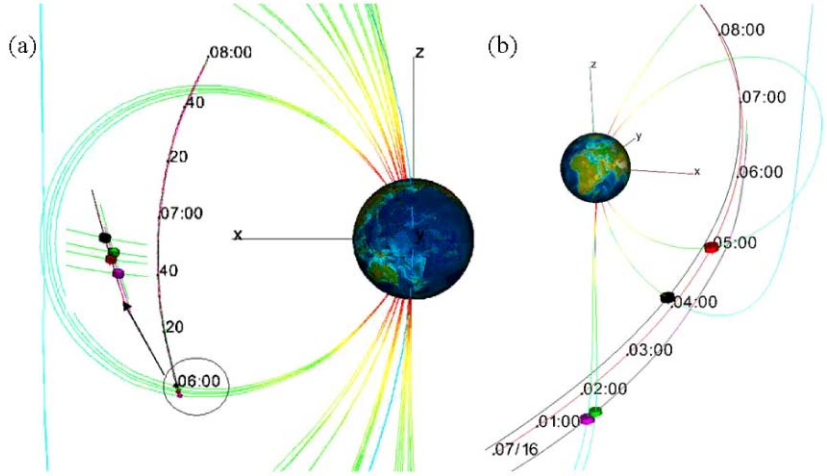

Fig. 6 Orbit tracks and constellation produced with the Orbit Visualization Tool (OVT, http://ovt.irfu.se). Magnetic field lines intercepting each satellite are shown, as well as a shell of outermost magnetospheric field lines. The model field is a combination of IGRF internal field model and Tsyganenko 87 external field model. The colour code along field line indicates magnetic field intensity. (**a**) 26 September 2003, 06:00–08:00 UT, small separation mission phase (200 km), solar magnetic (SM) coordinate system. (**b**) 16 July 2005, 01:00–08:00 UT, multi-scale mission phase (10 000 km and 1000 km), geocentric solar magnetospheric (GSM) coordinate system

of the four satellites in solar magnetic (SM) coordinates on 26 September 2003. The small spacecraft separation (200 km) does not allow distinguishing the four orbits, nor the four spacecraft, which travel from South to North. From the enlarged CLUSTER configuration shown in an insert, C1 (black) is ahead of C3 (green), C2 (red) and C4 (magenta). Figure 6b illustrates a multi-scale configuration on 16 July 2005, when the pair C3 and C4 (1000 km separation) is in the polar cap. At the same time, C1 is in the outer plasmasphere and C2 near the plasmapause.

4.1.2 Typical Spectral Signatures

Trapped continuum signatures are commonly observed in the low frequency range of WHISPER (Décréau et al. 2004). They present the smooth, large band spectral features already reported from the first observations (Gurnett 1975). It is in the "escaping continuum" frequency range (>∼20 kHz) that the CLUSTER multi-view offers the best opportunities to improve our understanding of this radio emission. In this range, NTC waves can be classified according to four main types: (i) "equatorial spots", (ii) "narrow band elements", (iii) "continuum enhancements" and (iv) "wide banded emissions". Those names refer to spectral signatures, which depend on two elements: the source on one hand (position, beaming properties and main frequencies) and the observatory on the other hand (position and movement). When the observatory moves rapidly in the vicinity of a source, spectral signatures inform about position and beaming properties of the source. In contrast, a remote observatory can be illuminated by a large region, hence perceive movements of sources via the spectral signatures it records. Visions about time or space in the resulting spectrograms are thus created by one or the other of the protagonists.

The first type of NTC spectral signature, the equatorial spot, is an emission limited in time (∼30 minutes) and frequency (∼10–30 kHz). In the spectrogram on Fig. 7a, harmonics

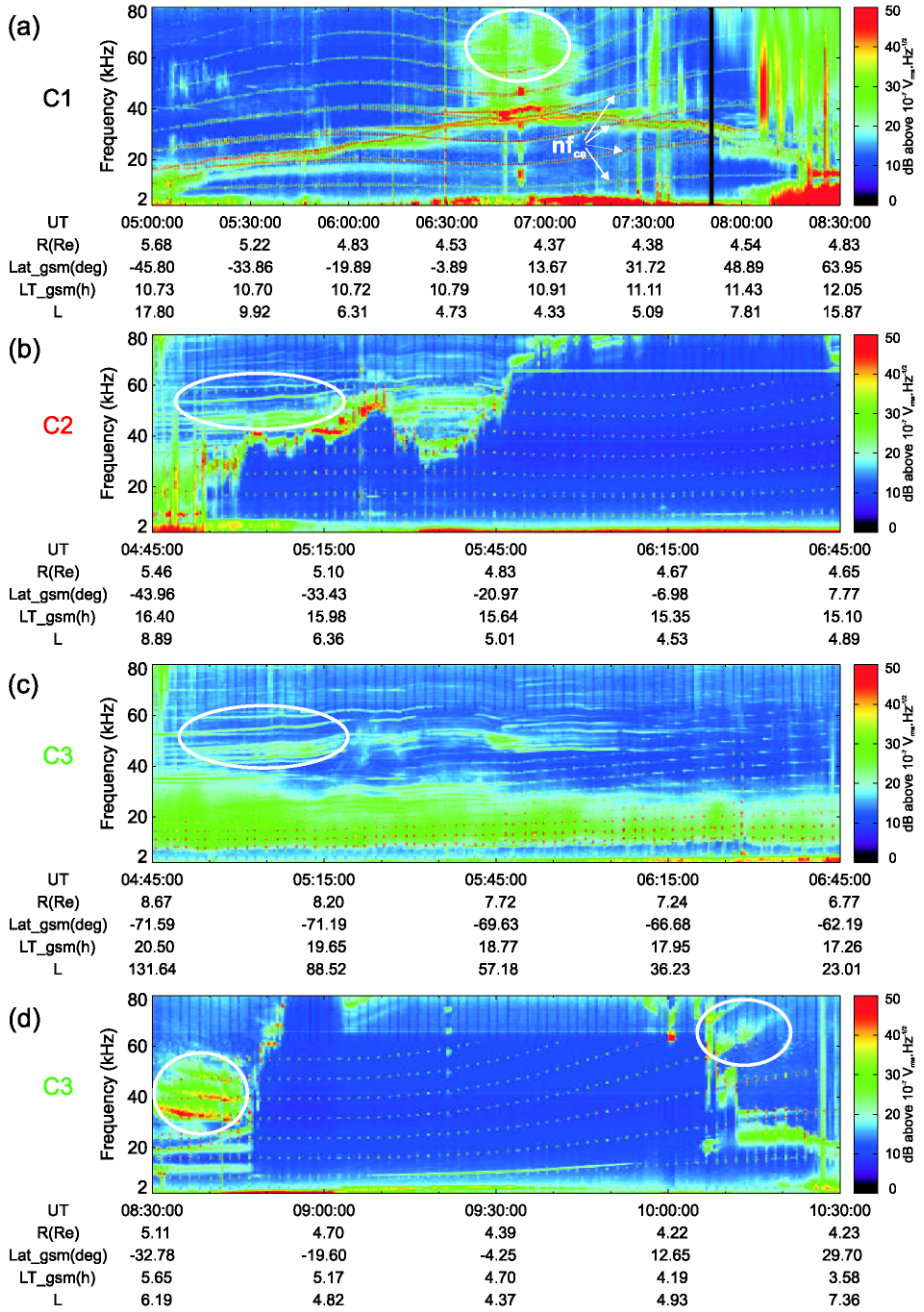

Fig. 7 Three main types of NTC spectral signatures (*white ovals*) observed with CLUSTER near perigee. (**a**) 26 September 2003, "equatorial spots"; (**b**)–(**c**) 16 July 2005, "narrow band elements"; (**d**) 30 December 2003, "wide banded emissions". CLUSTER constellation is shown in Fig. 6a for events presented in panels (**a**) and (**d**), in Fig. 6b for events presented in panels (**b**) and (**c**). *L* parameter values are calculated from the same magnetic field model than used by the OVT tool producing displays shown in Fig. 6.

of the electron gyrofrequency f_{ce}, triggered by regular sounding operations, appear as intense electrostatic emissions (small red points at ∼8–12 kHz and harmonics). Other resonant frequencies (red points between electron gyroharmonics) are the electron plasma frequency f_{pe} and the upper hybrid frequency f_{uh}. Their frequency position follows the increase of f_{pe} from 10 to 35 kHz (05:00–06:55 UT), and its decrease from 35 to 15 kHz (06:55–08:30 UT). The magnetic equator, at ∼06:55 UT, can be inferred by brief encounters of natural electrostatic emissions at $(n + \frac{1}{2}) f_{ce}$ below f_{pe}. It is worth noting that recent advances on electrostatic wave emissions at $(n + \frac{1}{2}) f_{ce}$ in the equatorial plasmasphere have been derived from CLUSTER data and detailed in El-Lemdani Mazouz et al. (2009). NTC emissions (above f_{pe}, in the frequency range 35–80 kHz) are observed on both sides of the equator between 06:35 and 07:10 UT. Time intervals when similar NTC spectral features are observed correspond most often to CLUSTER located near equator. We shall call this type of NTC emissions equatorial spot in short, standing for "near equatorial time-frequency intervals of radio emissions". This is a case when the observatory moves rapidly in the vicinity of a source region and spectral signatures inform about beaming properties.

The second type is the classical narrow band element form (Kurth et al. 1981), covering about 1 kHz or less. Such emissions appear often in series of waves at frequencies separated by a few kHz from each other, evolving together during time intervals of long duration (up to several hours). Spacing between frequencies f_n of related elements are arranged in quasi harmonic form, $f_n = (n + d) f_{ce}$ with $0 < d < 1$ and n an integer, f_{ce} being interpreted as the gyrofrequency at the source (Kurth 1982; Gough 1982). Figures 7b–c display narrow band NTC elements (40–60 kHz) observed identically and simultaneously (04:45–05:40 UT) by two different CLUSTER spacecraft located at different positions: C2 enters in the plasmasphere, while C3 is placed in the polar cap (see Fig. 6b for the configuration of the constellation).

The third type of NTC spectral form, the continuum enhancement, has been reported for the first time by Gough (1982). It develops after the start of an electron injection event, its spectral shape evolving over duration of one to several hours (Kasaba et al. 1998). Analysis of one example, observed by CLUSTER in the night sector, indicates that a region source of large dimension might be involved (Décréau et al. 2004). This form has not yet been identified by CLUSTER at perigee, either because it travels too fast in comparison to the typical time scale of the event, or because it is not placed at sufficient distance to be illuminated adequately by the various sources, which are likely at play. Indeed, the continuum enhancement scenario proposed by Gough (1982) and Kasaba et al. (1998) involves injection of electrons followed by a plasmapause inward convection. The wave sources (which are where the injection meets the plasmapause) drift likely inward and eastward. This is a case when, in order to be illuminated by the large region engulfing all successive positions of the sources, the observatory has to be remote. Numerous observations of continuum enhancements, often associated with AKR emissions, have been done by CLUSTER on the outermost part of its orbit. Some observations are also available from over the polar cap.

A fourth spectral form, the wide banded emission, has been observed for the first time with CLUSTER (Grimald et al. 2008). It consists of one or several banded emissions with a frequency separation (5–10 kHz) of the order of f_{ce} values encountered at plasmapause. When several bands are observed, they peak at harmonics of the same frequency, interpreted to be the gyrofrequency at the source. For the event presented in Fig. 7d, they appear when the observing satellite approaches the flank of a thick plasmasphere, bounded by a narrow plasmapause. Events of this type have been observed only a few times per year. They are always associated with density steps of large amplitude encountered over short distances. Some are observed on the flanks of a cusp.

4.2 Analysis

4.2.1 Beam Stability

As noted above, the limited time duration of CLUSTER observing the equatorial spots is not due to inherent time duration of the emission, but mainly to the time evolution of CLUSTER view point over the source. Indeed, a satellite observes the radiation only when it is placed inside the illumination cone formed in space by the radiated beams. From a small constellation skimming the outer plasmasphere, compared wave intensities measured at fixed frequency on the four spacecraft indicate most often that the differences observed on intensity versus time profiles are simply due to time shifts between spacecraft progressing along orbit tracks, generally close to each other. When crossing a beam illuminating a limited cone angle in space, each spacecraft observes an increase of intensity followed by a decrease (Fig. 8a). Times of maximum intensity correspond to times when the spacecraft reaches the central part of the beam. When intensities are plotted with respect to *MLAT* (Fig. 8b), their maxima are aligned with each other, indicating that the beam did not move significantly between the first and the last crossing, which are separated by 5–10 minutes. A different behaviour is obtained when time variations at the source are taking place, as illustrated in Fig. 9. For this event, narrow band elements contribute to an equatorial spot observed from ∼11:00 to 11:30 UT in the 60–80 kHz frequency band. The frequencies of elements are modulated at a time period of about 6 minutes. The bottom panel of Fig. 9, comparing intensities measured by the four spacecraft at 80 kHz, indicates three consecutive increases of intensity observed simultaneously on the four spacecraft in the southern hemisphere. Such a signature indicates a temporal evolution of the radiation properties. In contrast, intensity versus time profiles observed in the northern hemisphere (peak intensities observed as shifted in time) correspond to a beam stable in time and space.

4.2.2 Beam Geometry

The multipoint view obtained from the CLUSTER constellation yields, at least partially, an image of beam contours in space. This capacity enables to test one theory of NTC beam formation, under which the beam geometry is constrained. Indeed, in the frame of the radio window theory examined and proposed by Jones (1980), mode coupling occurs between intense upper hybrid waves produced by a warm loss-cone component of energetic electron distribution and the cold-plasma Z-mode branch of the dispersion relation. Propagation into

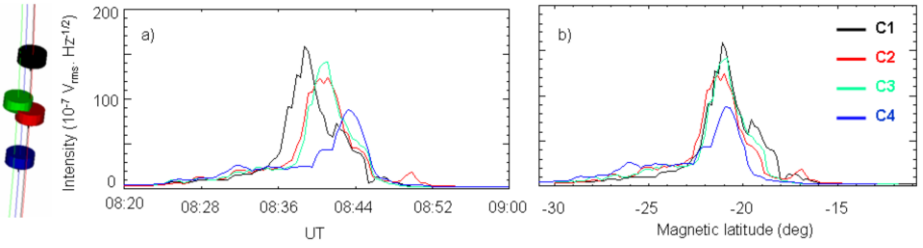

Fig. 8 Compared intensity variations at constant frequency (39.5 kHz), measured respectively by the four CLUSTER spacecraft when progressing along their orbit on 30 December 2003, (**a**) as a function of UT time, (**b**) as a function of magnetic latitude (constellation configuration shown at *left*). The corresponding beam is stable in space. (Adapted from Grimald et al. 2008)

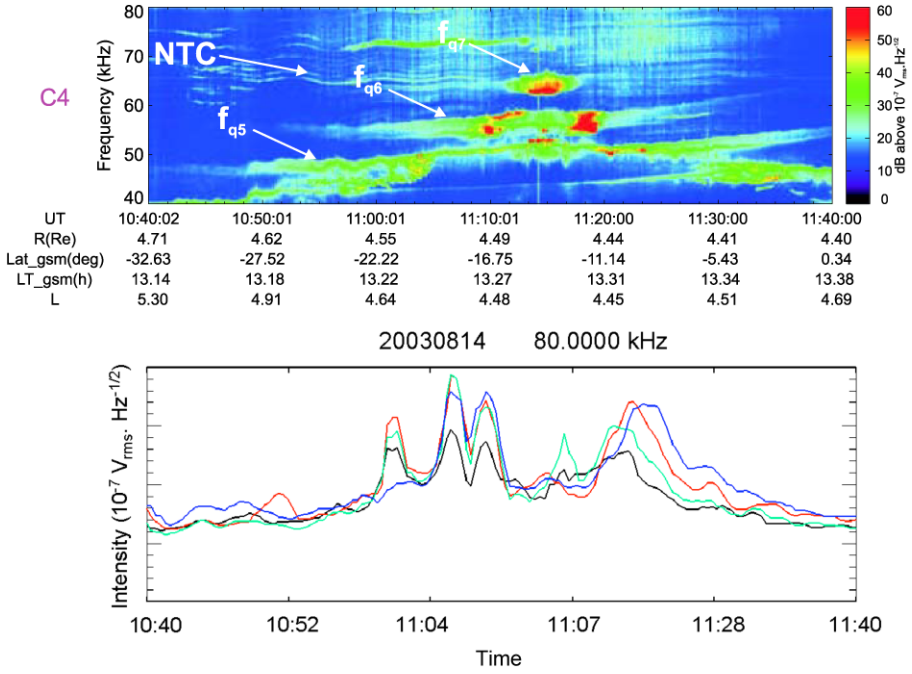

Fig. 9 (*Top*) Dynamic time electric field spectrogram of C4 for the 14 August 2003 event. Geomagnetic equator is crossed at about 11:15 UT (latitude is not expressed in SM coordinate system). NTC elements (electromagnetic waves) and a local emission (electrostatic Bernstein mode) are pointed with *arrows*. (*Bottom*) Compared intensity variations at a given frequency with *colour codes* and constellation configuration as for the event shown in Fig. 8

a slowly varying plasma density medium allows direct coupling of energy to L-O-mode waves, which propagate to lower density regions and beam away from the magnetic equator. According to this theory, the inclination angle of the beam with respect to magnetic equator is fixed by the ratio f_{ce}/f_{pe} of characteristic frequencies at the source. The source, placed at the equator (minimum in magnetic field value) radiates two beams, one in each hemisphere. The cone angle attached to each beam is typically $\sim$1–2° large (see Fig. 10a adapted from Jones 1982).

A test of validity of radio window theory (Grimald et al. 2007) has been performed in the case event presented in Fig. 7a, where the equatorial spot NTC form displays two intensity peaks, placed symmetrically to the magnetic equator, a feature, which could be attributed to the symmetrical beams displayed in Fig. 10a. This study could not draw a definitive conclusion about the validity of Jones theory. Indeed, the radio theory is compatible with quantitative observed beaming properties of a selected frequency element when an ad-hoc choice of source position in latitude is made. Although the latitude obtained thus (less than 1° off the equator) is in the expected range, the complete picture does not fit the narrowness of the beam indicated by the theory. Figure 10c displays orientations of the ray path of the 70 kHz NTC wave measured from intensity spin modulation at successive positions of the observing spacecraft on their orbit (curved arrows). Ray path orientations and orbit paths are shown projected onto the XY GSE plane, parallel to the spin plane. One insight in the third dimension is provided by the choice of two different line colours: Ray paths obtained from C4 in southern hemisphere are plotted in blue, whereas ray paths obtained from C2 in

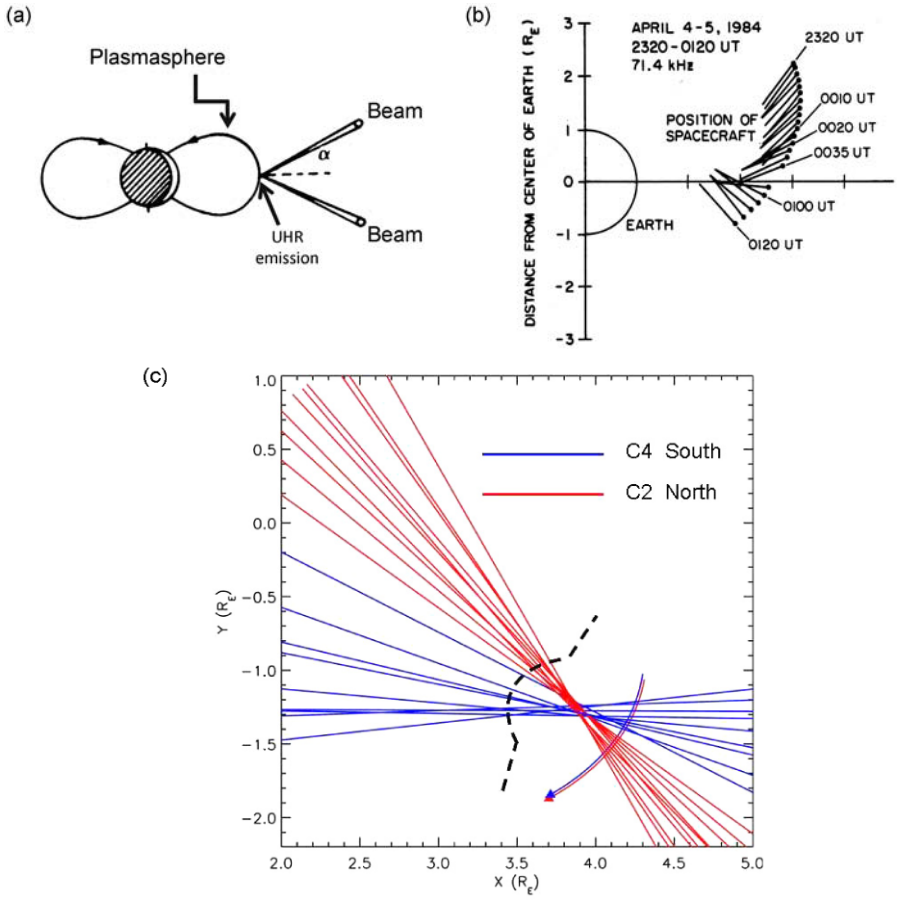

Fig. 10 Beaming properties of NTC waves: (**a**) configuration of NTC beams expected from the radio-window theory (adapted from Jones 1982); (**b**) ray path directions in a meridian plane derived from directivity measurements onboard DE-1 (adapted from Morgan and Gurnett 1991); (**c**) ray path directions of NTC element at 69 kHz derived from CLUSTER and drawn in *blue* for C4 in the southern hemisphere, in *red* for C2 in the northern hemisphere (in XY GSE plane); sketch of a possible associated plasmapause shape (*dotted line*); orbit elements of C2 and C4 shown by the *red* and *blue curves* with *arrows*. (Adapted from Grimald et al. 2007)

northern hemisphere are plotted in red. In this 2-D view, all ray paths point towards the same region, but the point of view drifts from negative ($\sim -4°$) to positive ($\sim +4°$) latitudes along the orbit element considered, which at the same time drifts of about 8° in GSE longitude (but less, below 3°, in SM longitude, corresponding to MLT). As a consequence, the sketch of Fig. 10a, which represents a meridian cut at fixed MLT, cannot be directly compared to observations. Narrow beams (of cone angle $<1°$) emitted from a single source could not be visible over such a large portion of the orbit. Furthermore, complementary observations detailed in Grimald et al. (2007) indicate that the orbit track is illuminated by several sources of small dimension and various frequencies, placed at different latitudes along roughly the same magnetic field tube, hence concentrated, after projection to the XY GSE plane, within a small area.

4.3 Interpretation

4.3.1 Main NTC Form (Quasi Equatorial Sources)

Close up View on Sources Intense electrostatic emissions at NTC frequencies are encountered in the plasmapause region (Kurth et al. 1981). They are thus considered as potential electrostatic sources radiating energy (likely by wave decay or linear conversion) in the form of continuum waves of electromagnetic nature. No simultaneous observations of such a NTC source by one CLUSTER spacecraft and of the beam emitted from that source by another spacecraft has been found. This is due to the 3-D nature of the geometry involved, the small size of sources and the limited extension of the beam near sources. Then, it has not been possible so far to directly test a generation mechanism by comparing wave characteristics at both ends of the process.

The spectrogram of Fig. 9 provides nevertheless an insight on the frequency, size and position of candidate electrostatic sources in the equatorial region. The magnetic equator is crossed at 11:15 UT when f_{pe} (narrow feature in yellow) culminates at ∼53 kHz. Above that frequency, WHISPER observes banded electrostatic emissions displaying upper frequency cut offs at the Bernstein frequencies f_q characteristic of the harmonic band considered. The intense spots (in red) showing up in the spectrogram of Fig. 9, one at ∼64 kHz at the equator, and two at ∼55 kHz on both sides of the equator, belong to the bands associated to Bernstein modes, the $[6f_{ce}-f_{q6}]$ frequency interval in the latter case and the $[7f_{ce}-f_{q7}]$ interval in the former case. These spots are candidate sources, which could participate to the generation mechanism proposed by Rönnmark (1985). Lastly, an event observed on 30 May 2003 by Canu et al. (2006), where NTC frequencies oscillate with time at similar periods than the central frequency of local Bernstein band series, completes this view. The authors interpretation is that Bernstein emissions probably play a role in the generation of NTC radiations.

A striking characteristic of NTC spectral signatures observed near the plasmapause is their splitting in fine structures. This property has been pointed out by detailed analysis of the waves forming the equatorial spots (Grimald et al. 2007). Complex spectral features of NTC observed in Fig. 9 can be interpreted as produced by a superposition of beams emitted from many sources, placed at different locations along the plasmapause and near the equator.

Ray path observations made by DE-1 while skimming the outer plasmasphere (Morgan and Gurnett 1991) can be usefully compared to CLUSTER observations (Grimald et al. 2007). Both views are complementary: DE-1 provides a view in a meridian plane and CLUSTER in the equatorial plane. The ray path directions obtained from DE-1 are more or less parallel to each other during intervals of significant duration, here from 23:20 to 00:20 UT (Fig. 10b). This could be due to sources placed in the equatorial plane at various geocentric distances. An alternative explanation is that the topology observed is due to sources placed at similar geocentric distances but at different latitudes along a single flux tube. The latter interpretation makes better sense in view of CLUSTER observations, which indicate a source region concentrated at a single geocentric distance and emitting beams inside a cone of large longitudinal extent, ∼40° (Fig. 10c). Such a large extent, similar to longitudinal cone angle of KC radiations (Fig. 4), cannot be envisaged to be produced by a plasmapause boundary smooth in azimuth. This ray path topology is not unique but representative of similar events. It could be due to a particular shape of the plasmapause, known to display density irregularities in azimuth (Darrouzet et al. 2006). In particular, ray paths being likely aligned with density gradients (Jones 1982), a small bite-out structure, sketched

in Fig. 10c, could act as a collimator concentrating radiations. This scenario would be similar to the interpretation of KC emissions proposed by Green et al. (2002) and illustrated in Fig. 2.

Propagation Effects Statistics of occurrence at CLUSTER orbit of equatorial spots and narrow band elements indicate that they are probably signatures of the same phenomena, observed from different perspectives (Grimald 2007). The underlying scenario implies wave propagation. A ray tracing study considers the fate of waves emitted from equatorial plasmapause at a given inclination angle with respect to the equatorial plane, after they have been reflected by the magnetopause density wall (Green and Boardsen 1999). Ray tracing indicates latitudinal confinement of NTC radiation emitted at small inclination angles, since those waves do not move at large distance from the equatorial plane and stay trapped between the plasmapause and magnetopause density walls. In contrast, rays emitted at higher inclination angles bounce at magnetopause, but escape a second bounce at plasmapause as they travel above the poleward plasmasphere regions. Such a scenario explains observations of narrow band elements by C3 during the event of 16 July 2005 (spectrogram in Fig. 7c): C3 is placed above the South Pole, Fig. 6b showing CLUSTER satellites positions at 05:00 UT. At that time, C3 observes a narrow band element at ∼60 kHz, observed more faintly by C2 at about 40° south latitude (Fig. 7b). Directivity analysis indicates that corresponding ray paths point both towards dayside magnetopause. The interpretation proposed in Grimald (2007) is that a common source placed near equatorial plasmapause emits a 60 kHz wave in a beam of large enough latitudinal cone angle to illuminate the four CLUSTER spacecraft after a bounce at magnetopause (spectrograms for C1 and C4, not shown, display similar narrow band spectral features). This case event demonstrates that narrow band NTC elements can illuminate large regions of the magnetosphere placed at significant distance from the equator without loosing their characteristic spectral features. The magnetopause-magnetosheath boundary, populated by complex density structures, could play a role in angle scattering. According to the above scenario, the cohesion in latitude and frequency of the equatorial spots observed in the near equatorial outer plasmasphere is lost during propagation. Only the elements emitted at highest inclination are preserved from being trapped and superposed to radiations from other sources. Among those, only the elements emitted at highest intensity would keep a sufficient level to be observable after propagation.

4.3.2 Wide Banded NTC Emissions

NTC wide banded emissions (Fig. 7d) display a spectral pattern shown in better details in Fig. 11. They present two remarkable characteristic signatures, which, combined, allow

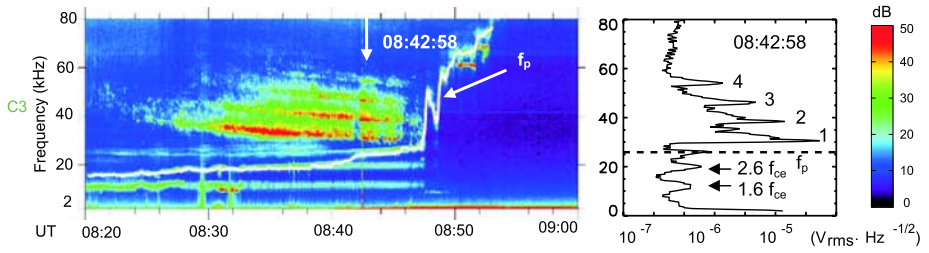

Fig. 11 WHISPER spectrogram on 30 December 2003 and individual frequency spectrum displaying four peaks above plasma frequency. (Adapted from Grimald et al. 2008)

to propose a precise location of the corresponding radio sources. The first characteristic signature is their frequency pattern, peaking at exact harmonics of a fundamental frequency, which is interpreted as the gyrofrequency at the source region. The second characteristic is the evolution of the fundamental frequency with respect to the view point of the observer, indicating that the NTC beams are narrowly collimated. During this event, C3 travels in the outer plasmasphere region, southern hemisphere, from 08:20 to 08:47 UT, at which time it crosses the plasmapause (Fig. 11). The other satellites cross the plasmapause within a few minutes time span. They form together a constellation of small size, C1 and C4 being ∼1200 km apart. The crossing area is placed at a ∼4.85 R_E geocentric distance, at $MLAT \approx 20°$ and ∼04:36 MLT. The f_{pe} measured by C3, plotted as a white solid line over the spectrogram, follows large density irregularities at plasmapause crossing, which can thus be better qualified as a structured plasmasphere boundary layer, PBL (Carpenter and Lemaire 2004). NTC emissions, present from ∼08:27 to 08:47 UT, form three clear bands (a fourth one is visible after 08:40 UT). An individual spectrum is shown on the right panel, where peaks of the four bands are labelled from 1 to 4. Compared observations of the four satellites demonstrate that the NTC beams encountered are stable in time and confirm that they are limited to a cone of small angle.

All peaks are placed at exact harmonics of a value df, which slowly decreases with increasing $MLAT$ of observation. The frequency pattern observed contrasts with previous views, where frequencies emitted in a region of gyrofrequency f_{ce} are supposed to satisfy $f_n \approx (n + \frac{1}{2}) f_{ce}$ (Kurth 1982), not $f_n \approx n f_{ce}$. An additional experimental fact is the evolution of the NTC fundamental frequency encountered along the orbit element. The frequency df of the spectral pattern is higher than local gyrofrequencies and the difference progressively diminishes, until df meets local gyrofrequency at the plasmapause. This behaviour is the same in all observations of NTC features of the wide banded form. The spectrogram in Fig. 7d shows indeed another example in the northern plasmapause crossing of the same orbit. The interpretation proposed by Grimald et al. (2008) is that sources are placed at the intersection of the plasmapause magnetic shell (at $L \approx 5.5$ in this case) and of isogyrofrequency surfaces, leading to source positions at $MLAT \approx 20°$. This latitude is clearly higher than in the generally accepted view of equatorial sources. Together with the uncommon spectral characteristics (wide banded emissions, peaks at exact harmonics), it is possible that the generation mechanism is specific to that particular type of continuum radiation. A theory describing direct generation of electromagnetic O-mode emission at exact electron gyroharmonics, via mildly energetic electron beams in highly dense and warm plasma, has been proposed by Farrell (2001). CLUSTER observations could be related to this mechanism, and thus be a first confirmation of it.

5 Z-Mode

5.1 Active Z-Mode Experiments in Space Plasmas

Many spacecraft have generated Z-mode waves in the ionosphere and magnetosphere using radio sounders, among them the ISIS satellites and the OEDIPUS sounding rockets (e.g., Benson et al. 2006). This work has provided a powerful complement to observations of Z-mode waves of magnetospheric origin performed on rockets and satellites using plasma wave receivers (e.g., LaBelle and Treumann 2002). In this section we describe Z-mode experiments from IMAGE that provide new perspectives on the use of radio sounding at altitudes exceeding those accessible to previous missions and under comparatively more favorable conditions on transmitted frequencies and maximum observable echo delay.

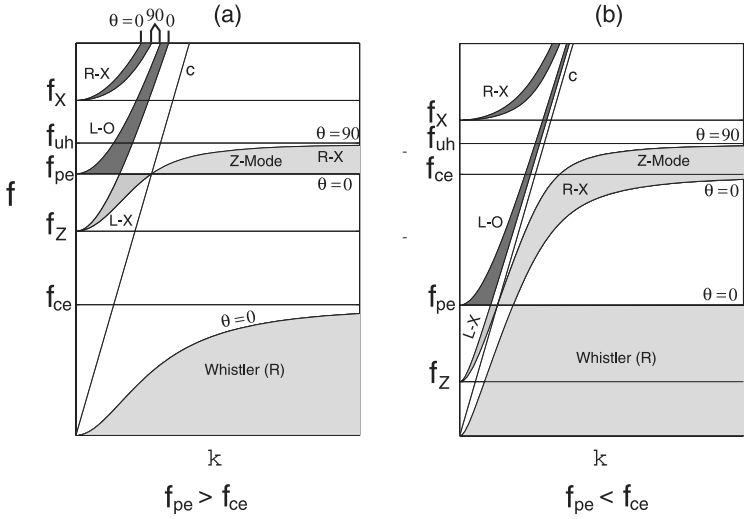

Fig. 12 Dispersion diagrams for waves in a cold plasma illustrating two conditions on the ratio of electron plasma frequency to electron gyrofrequency: (**a**) $f_{pe} > f_{ce}$ and (**b**) $f_{pe} < f_{ce}$. (Adapted from Goertz and Strangeway 1995)

By way of introduction to the IMAGE experiments, we show in Fig. 12 a schematic diagram that represents the dispersion relation for waves in a cold plasma, i.e., the scalar relation expressing the angular frequency ω in terms of the propagation vector $\boldsymbol{k}$, which is related to the refractive index $\boldsymbol{n}$ by $\boldsymbol{n} = \boldsymbol{k}c/\omega$. The diagrams represent two conditions on f_{pe}/f_{ce}, the ratio of electron plasma frequency to electron gyrofrequency. The case of $f_{pe} > f_{ce}$, represented in Fig. 12a, is typical of the plasmasphere above several 1000 km altitude, while the condition $f_{pe} < f_{ce}$, in Fig. 12b, is common at low altitudes poleward of the plasmapause and within a limited altitude range near 2000 km in the mid-latitude topside ionosphere.

5.2 Z-Mode Sounding from IMAGE

When the RPI instrument onboard IMAGE operates at altitudes above ~20 000 km, its entire frequency range from 3 kHz to 3 MHz may fall within the domains of the free-space L-O and R-X wave modes (see Fig. 12). However, as the satellite moves to lower altitudes, some part of its operating frequency range begins to fall within the Z-mode and whistler-mode domains, and thus provides the possibility of using those wave modes to probe the plasmasphere and polar regions at altitudes less than ~10 000 km. In response to this opportunity, new Z- and whistler-mode probing tools have been developed that complement the operation of RPI at higher frequencies as a conventional sounder. In this section we discuss three basic types of Z-mode echo activity: (i) ducted waves that are presumably constrained by field-aligned irregularities (FAI) to follow the direction of the magnetic field $\boldsymbol{B}$, (ii) non-ducted or "direct" echoes that follow ray paths extending in generally Earthward directions, (iii) scattered echoes that are believed to return to the spacecraft following interactions with FAI located in directions generally transverse to $\boldsymbol{B}$ from IMAGE. Comments on use of the echoes as plasma diagnostic tools will follow. We begin with the newly discovered phenomenon of bidirectional sounding along geomagnetic field lines using ducted Z-mode waves (Carpenter et al. 2003).

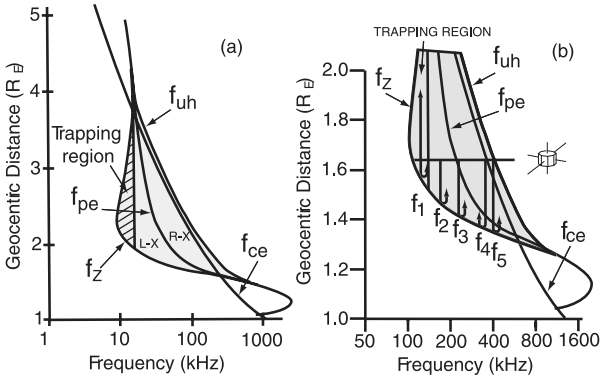

Fig. 13 (**a**) Model plot of the variation of key plasma parameters with geocentric distance along polar region field lines, showing by shading the Z-mode propagation cavity or trapping region. (Adapted from Gurnett et al. 1983.) (**b**) Number of idealized ray paths for Z-mode echoes in a particular case of sounding by RPI near $L = 3$ in the plasmasphere. (Adapted from Carpenter et al. 2003)

5.2.1 Ducted Echoes and the Z-Mode Propagation "Cavity"

Since plasma parameters such as f_{pe} and f_{ce} are known to decrease monotonically with altitude above the peak of the ionospheric F layer, and since the cutoff frequency f_Z for Z-mode propagation in a cold plasma is expressed in terms of f_{ce} and f_{pe} as:

$$f_Z = (f_{ce}/2)\left[-1 + \left(1 + 4\left(f_{pe}/f_{ce}\right)^2\right)^{\frac{1}{2}}\right], \tag{1}$$

one might expect f_Z to decrease monotonically with altitude as well. This is not true, however, as a number of authors have emphasized (Gurnett et al. 1983; LaBelle and Treumann 2002). In an altitude range extending from ~1500 km to above 5000 km, a Z-mode propagation "cavity" regularly exists over a wide range of latitudes. Waves originating at frequencies "within" the cavity can return from reflection points both above and below the wave source. This occurs in spite of the fact that the higher altitude reflection takes place in a plasma region less dense than the one at the source.

Figure 13 illustrates the cavity effect by altitude profiles of two frequencies, f_Z and f_{uh}, which (as shown in Fig. 12) locally delimit Z-mode propagation in a cold plasma. Also plotted versus geocentric distance are models of the plasma parameters f_{ce} and f_{pe}. The left-hand diagram was used in a study of natural wave activity in the auroral region, while the right-hand diagram represents conditions encountered by RPI during sounding operations at middle latitudes. It is clear that the curve for f_Z undergoes a minimum with altitude and that the minimum is reached within an altitude range in the topside ionosphere where the ratio f_{pe}/f_{ce} falls to a minimum value near or below unity. In Fig. 13a, hatching shows a range of frequencies at each altitude for which locally launched waves could be expected to return after reflection from points both above and below the source. Figure 13b shows schematically the propagation paths of a sequence of waves launched by RPI over a range of frequencies f_i from f_Z to f_{uh}. Waves at frequency f_1, just above f_Z, remain within the cavity and are reflected from both above and below RPI. In contrast, frequencies f_2, f_3, and f_4 exceed the upper frequency limit of the cavity and the corresponding waves reflect only at points below the spacecraft (assuming propagation in the general direction of $\boldsymbol{B_0}$).

Two examples of propagation within a cavity are illustrated in Figs. 14a–b on plasmagrams. On both records there is a band of no electromagnetic propagation at the lower frequencies, followed by a broad belt of noise that is attributed to a combination of scattering of RPI Z-mode pulses from irregularities located in directions generally transverse to $\boldsymbol{B_0}$

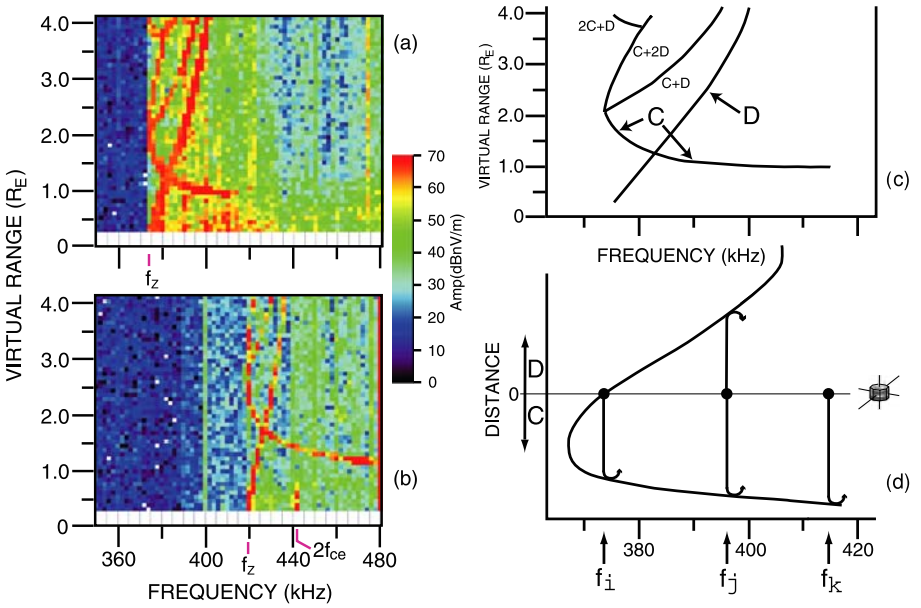

Fig. 14 (**a**)–(**b**) RPI plasmagrams from 28 July 2001 showing echo intensity in coordinates of virtual range (echo range at an assumed propagation velocity of c) versus transmitted frequency. Multicomponent Z-mode echoes are detected within the plasmasphere on successive soundings 2.5 minutes apart. (**c**)–(**d**) Interpretive model of the echoes of panel (**a**) for the case of a sounder location above the minimum in Z-mode cutoff frequency with altitude. The horizontal scale has been expanded by a factor of ∼2 to facilitate comparisons of echo delays. (Adapted from Carpenter et al. 2003)

(Muldrew 1969; Sonwalkar et al. 2004) as well as Z-mode noise from distant sources (Benson and Wong 1987; Benson 1993). The local Z-mode cutoff f_Z is found to be at or near the low-frequency edge of this band. Clearly outlined against the background noise are patterns of discrete echo traces that begin at f_Z.

An interpretation of the propagation paths of the discrete echoes shown in Fig. 14a is presented in Figs. 14c–d. Panel (**c**) is a rescaled tracing of the echo observed in Fig. 14a, while panel (**d**) shows on the same frequency scale the variation with altitude of f_Z in a postulated propagation cavity. The sounding is assumed to have taken place at an altitude above the minimum value of f_Z in the cavity. The upward and downward directions of propagation are identified as D and C, respectively. As the sounder frequency steps upward and reaches f_Z at ∼372 kHz, an echo f_i is received from a reflection altitude below IMAGE, forming the first elements of what becomes the down-sloping C echo trace. As the sounder continues above f_Z, echoes such as f_j begin to return from both higher and lower altitudes. The D echo forms near zero range and extends rapidly towards longer delays because of the small spatial gradients in f_Z encountered in the upward direction. Finally, the sounder frequency exceeds the peak value reached by f_Z above IMAGE, after which echoes such as f_k can return from below only.

The remarkable clarity of the echo traces suggests that the signals involved were guided or ducted by geomagnetic FAI, a phenomenon that has been found necessary to explain ground-observed whistler-mode signals (Smith 1961; Helliwell 1965). Ducting has recently been invoked to explain discrete O- and X-mode propagation from RPI (Reinisch et al. 2001; Fung et al. 2003) and was earlier identified from observations with ISIS satellites (Muldrew

1963; Loftus et al. 1966). The existence of a single discrete propagation path passing through the satellite position is indicated by the additional components in Fig. 14a identified as C+D, C+2D, and 2C+D in Fig. 14c. Each of the higher order components consists of some combination of the measured delays along the original C and D paths.

When RPI launches Z-mode waves from an altitude below the minimum of a Z-mode cavity, a quite different echo pattern is detected, but again there are well defined echo components from upward and downward directions as well as combinations of the two in the manner of Fig. 14c. Thus it was concluded that an explanation of events such as that of Fig. 14a requires the existence of both a propagation cavity as well as the occurrence of ducted propagation along the magnetic field (Carpenter et al. 2003).

5.2.2 *Remote Sensing of Density Profiles Along the Geomagnetic Field Lines Above IMAGE*

The propagation cavity is of geophysical interest for a number of reasons. In the case of the D component in Fig. 14c, representing upward propagation along the geomagnetic field from IMAGE, an inversion technique can be applied to determine the electron density profile along the path up to the altitude limit reached by the measured D component (for the conditions of Fig. 13a, that limit was predicted to be $\sim 4\ R_E$). The inversion method, described in Carpenter et al. (2003) was applied in the cases of Fig. 14a and Fig. 14b with the results shown in Fig. 15 on a plot of plasma density versus *MLAT* for $L = 2.1$ and 2.3. Density is shown from the position of IMAGE upward to a point ~5000 km above IMAGE along $\boldsymbol{B_0}$. For comparison, we show a profile for $L = 2.3$ from an empirical model obtained by Huang et al. (2004), based on X-mode sounding by RPI along multiple field-aligned paths on 8 June 2001. This profile (dashed curve) was scaled by a factor of 0.8 in order to show how well

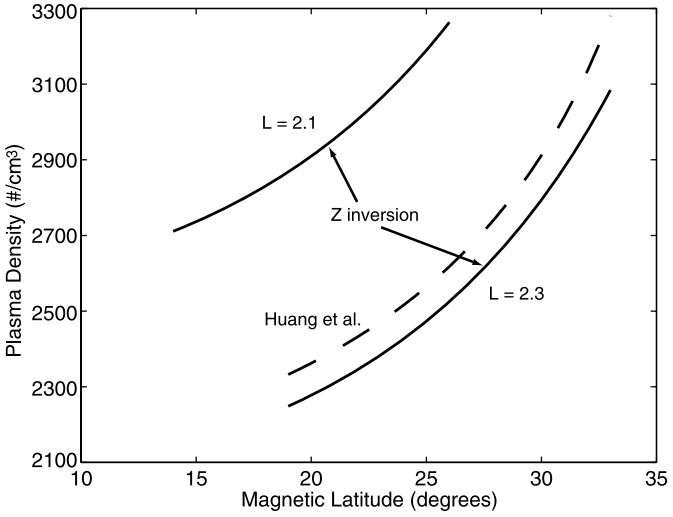

Fig. 15 Plots of electron density versus *MLAT* at $L = 2.1$ and 2.3, inferred from the upward propagating Z-mode signals illustrated in Figs. 14a–b and identified as component D in Figs. 14c–d. The *dashed curve* is for $L = 2.3$ from the Huang et al. (2004) model for a different date. That model is based upon inversion of free-space mode echoes that propagated to RPI along multiple field-aligned paths. (Adapted from Carpenter et al. 2003)

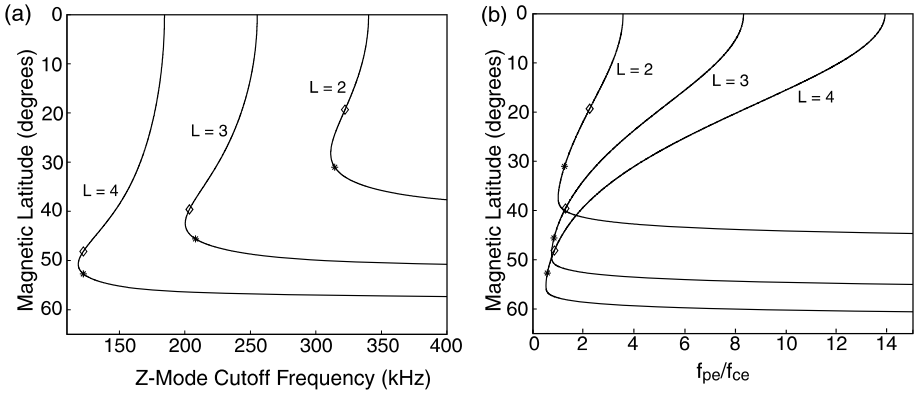

Fig. 16 (**a**) Plot of calculated Z-mode cutoff frequency f_Z versus *MLAT* along geomagnetic field lines at $L = 2$, 3, and 4, illustrating the widespread occurrence of a low-altitude minimum in f_Z within the plasmasphere. A dipole magnetic field model and a diffusive equilibrium density model were assumed. *Marks along the curves* show the locations of the 3000 km and 5000 km altitudes, respectively. (**b**) Corresponding plot for the ratio f_{pe}/f_{ce}. (Adapted from Carpenter et al. 2003)

the curves for $L = 2.3$ agree. Geomagnetic conditions relevant to the X (downward) and Z (upward) measurements ranged from calm (X profile) to quiet (Z profile) similar (near $L =$ 2.3, variations of 20–30% in the scale factor of the field-aligned electron density distribution with time, longitude, and disturbance levels are common (Carpenter and Anderson 1992)).

5.2.3 Remote Sensing of Plasma Composition Along the Geomagnetic Field Lines

The f_Z profile with altitude may be used as a diagnostic of plasma composition along $\boldsymbol{B_0}$ in the topside ionosphere region. If one assumes a three-component plasma in diffusive equilibrium above a reference altitude, a small positive electron temperature gradient along $\boldsymbol{B_0}$, and a known value of electron density at the magnetic equator, one then finds that in order to place a minimum in the f_Z profile in the 3000–5000 km altitude range where it has been observed, there are important constraints on the ion composition at the reference level.

Figure 16a is a plot of calculated f_Z profiles along $\boldsymbol{B_0}$ at three L values (2, 3, 4), with *MLAT* plotted on the vertical scale. In Fig. 16b are shown corresponding plots for the ratio f_{pe}/f_{ce}. Using the empirical model of electron density at the equator of Carpenter and Anderson (1992), an assumed ratio of He^+ to H^+ of 0.05 to 0.1 at the equator, an assumed value of 2 for the ratio of the electron temperature at the equator to the same temperature at the 1000 km reference level, it was found that a distribution of 82% O^+, 17% He^+ and 1% H^+ at the reference level would predict the profiles of Fig. 16a, which exhibit an f_Z minimum in the observed 3000–5000 km altitude range (Carpenter et al. 2003). The altitude of the minimum appeared to be sensitive to the choice of composition at the reference level, thus suggesting that further observations of this kind could be used to investigate the poorly known distribution of ions in the coupling region between the ionosphere and the plasmasphere.

Since little is known of the variations of the plasma properties along the geomagnetic field lines at altitudes below 5000 km, Z-mode probing of the kind described here can become a valuable adjunct to conventional radio sounding. The RPI data offer many as yet unexploited opportunities for application of the new method.

5.3 Additional Diagnostics Uses of Z-Mode Echoes

5.3.1 Non-Ducted or "Direct" Earthward Propagating Z-Mode Echoes

When IMAGE operated in the plasmasphere at $L < 3$ near 3000–4000 km altitude, the ratio f_{pe}/f_{ce} was frequently >1 but not $\gg 1$, and RPI was found to produce discrete, non-ducted echoes that followed ray paths extending generally Earthward from the satellite. Ducted echoes of the kind described above could also be present (as often happened in the outer plasmasphere in the case of simultaneous direct and ducted X-mode echoes). The direct Z-mode echoes represent low to medium altitude versions of phenomena familiar from topside sounding work (Carpenter et al. 2003).

Two examples of direct echoes recorded on 6 July 2001 are shown in Figs. 17a–b. They were recorded, respectively, at 3100 km altitude, $L = 2.4$ and at 4100 km altitude, $L = 2$. On both panels, a vertical spike identifies the local f_{pe}. There are two discrete Z-mode echoes, labeled Z and Z′. The Z′ trace begins at local f_{pe}, while the main Z trace rises slowly in travel time (range) from an origin at f_Z, inferred to be off scale to the left. The Z trace finally crosses over the Z′ trace and the two echoes then extend towards asymptotically long delays at a maximum frequency below f_{uh}. This maximum is associated with a limit on vertical incidence propagation (Jackson 1969).

5.3.2 Diagnostic Uses of Direct Z-Mode Echoes

The Z′ trace, as observed on topside sounders, was interpreted by Calvert (1966) as having propagated obliquely between the satellite and the O-mode reflection level at $f = f_{pe}$. The occurrence of two distinct Z-mode echo traces at $f > f_{pe}$ is a consequence of the anisotropy of the medium, such that ray paths involving two different initial wave normal angles can lead back to the satellite. The Z′ trace was explained by Calvert (1966) in terms of non-vertical propagation in a horizontally stratified ionosphere. The "reflection" does not occur at a Z-mode cutoff, but is in fact the result of refraction such that the ray path reverses direction at a level where $f = f_{pe}$. The Z′ trace can be expected to provide information that is independent of results obtained from inverting the regular Z-mode echo. Note that the trace delays are substantially longer than those of an O echo at common frequencies, accentuated by a Z-mode transition at f_{pe} from a fast mode to a slow mode. These traces are therefore more useful (given the minimum 3.2-ms RPI pulse length and receiver sampling frequency) than the O- and X-modes of the transitional altitude region. Analysis of Z and Z′ traces for particular RPI echo observations remain to be performed. However, the information on local f_{pe} provided by the Z′ trace is particularly helpful for plasma diagnostics at altitudes near 3000–5000 km in the plasmasphere, where the condition $f_{pe}/f_{ce} \approx 1$ is common and thus where estimates of f_{pe} based upon measurements of f_{uh} by passive probing may not provide desired accuracy.

5.3.3 Scattered Z-Mode Echoes

In the plasmasphere at altitudes such that the Z-mode frequency domain was broad enough to occupy a significant range of frequencies below f_{uh}, a background of diffuse Z-mode echoes was almost always present, whether or not discrete echoes were received. When discrete echoes were present, they were typically ∼20 dB above the levels of the diffuse background, as illustrated in Figs. 17a–b.

Plasmagrams from the low altitude polar regions where $f_{pe}/f_{ce} < 1$ regularly exhibited diffuse echoes with the forms illustrated in Figs. 17c–d. Distinctive features included:

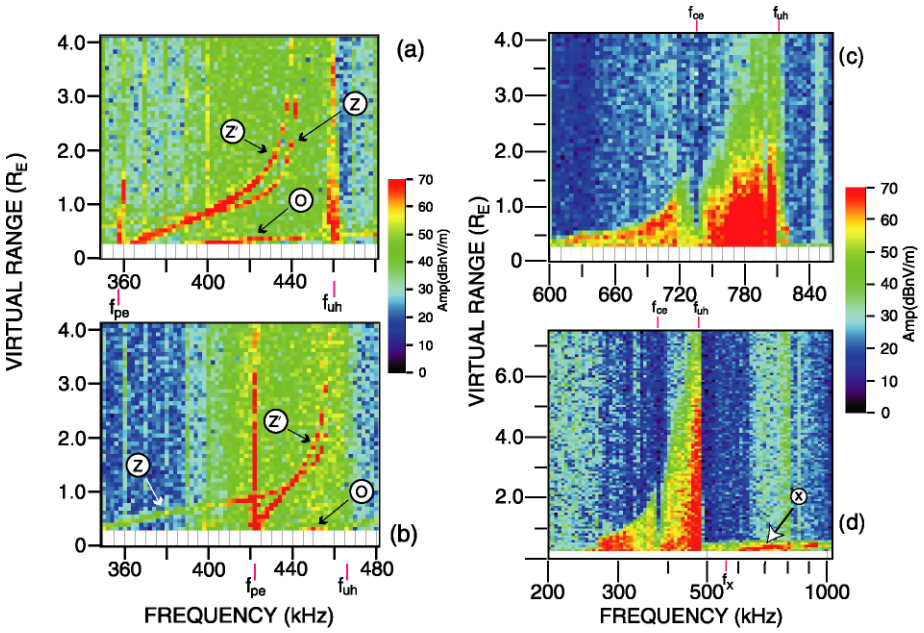

Fig. 17 (**a**)–(**b**) RPI plasmagrams illustrating Earthward propagating discrete Z and Z′ echoes seen against a background of diffuse Z-mode noise. (**c**)–(**d**) RPI plasmagrams typical of low altitude polar regions showing diffuse Z-mode echo activity useful for determining f_{ce} and f_{pe}. (Adapted from Carpenter et al. 2003)

(i) echoes with ranges substantially longer than those of order 0.5 R_E to be expected for Earthward propagating O- and X-modes, (ii) echo activity extending from the lowest detectable range to a maximum value that increased with sounding frequency, (iii) a gap or weakening of the echoes at an intermediate frequency, and (iv) a relatively abrupt upper frequency limit, inferred to be f_{uh}.

Sonwalkar et al. (2004) performed a ray tracing analysis of diffuse echo events such as those of Figs. 17c–d, finding that for Z-waves below f_{ce}, Earthward propagation to turning points in the general $\boldsymbol{B}$ direction could not be excluded, but such propagation could not explain the wide time spreading of the Z echoes and would in any case tend to be masked by them. The authors pointed out that because of the variation with altitude of the Z-mode refractive index surface, at any given frequency f below the local f_{ce}, Z-mode waves can spread out in all directions. Some of these waves, in particular those propagating in directions from IMAGE that are approximately perpendicular to $\boldsymbol{B_0}$ are scattered by FAI and can return to the satellite. Meanwhile, for frequencies between f_{ce} and f_{uh}, Z-mode propagation is allowed within a resonance cone that permits propagation in the direction roughly perpendicular to $\boldsymbol{B_0}$. These waves can also lead to echoes after scattering from FAI, as has been documented by topside sounders (e.g., Muldrew 1969; James 1979).

5.3.4 Diagnostic Uses of Scattered Z-Mode Echoes

In a case study similar to those of Figs. 17c–d, Sonwalkar et al. (2004) found that the observed echo delays could be explained by irregularities located within ∼20 to 3000 km

from IMAGE. The overall distribution of time delays was consistent with propagation theory. For frequencies above f_{pe} (true of most of the observed echoes in Figs. 17c–d) we have a slow Z-mode, with group velocity decreasing and time delay increasing with frequency for any given wave normal direction. Above f_{ce} and close to f_{uh}, the Z-mode becomes quasi-electrostatic and much longer time delays are expected, as observed. The weakening of the echoes at a frequency corresponding to local f_{ce} (Carpenter et al. 2003) is believed to be related to the change in refractive index surface from a closed to an open topology at f_{ce}, as discussed by Gurnett et al. (1983) and LaBelle and Treumann (2002).

In the polar regions at altitudes in the 1000–4000 km range, where f_{pe}/f_{ce} is typically <1, f_{uh} as observed through passive scanning may no longer be a useful source of information on f_{pe}, being dominated by the value of f_{ce}, and also because of interfering auroral noise that may be present near 1 MHz. In such cases, Z-mode echoes such as those in Figs. 17c–d can provide a useful means of measuring local f_{pe} through f_{ce}, indicated by the gap in echoes, and by the upper hybrid resonance spike, which is often marked by a an abrupt drop in intensity by $\sim$40 dB on its high frequency side.

6 Whistler-Mode Soundings at Altitudes Below ∼5000 km

New whistler-mode (WM) tools for probing at altitudes below $\sim$5000 km have been developed during work on data from the RPI sounder onboard IMAGE (Reinisch et al. 2000). These tools are based upon various physical mechanisms involved in the reflection and return propagation to IMAGE of WM waves transmitted by RPI. As described by Sonwalkar et al. (2009), these mechanisms include: (i) magnetospheric reflection (MR) at locations where the wave frequency is less than or equal to the local f_{lh}, (ii) specular reflection (SR) from the steep density gradients at the bottom side of the ionosphere, and (iii) multipath propagation and scattering due to the presence of density irregularities that are often field-aligned. In most cases, MR- and SR-WM echoes are distinguished by the distinct upper and lower limits on their frequencies, limits that depend on the value of the lower hybrid resonance at the altitude of the satellite. The two echo types also differ widely in terms of their frequency-versus-time properties, which can be separately explained through ray tracing in models of the plasma environment below $\sim$5000 km. Preliminary descriptions of echoes attributed to specular reflection, multipath propagation and scattering have been provided by Sonwalkar et al. (2009). Here we limit ourselves to a brief description of the various echoes and their apparent diagnostic potential.

6.1 Spreading of RPI Whistler-Mode Echoes in Time Delay

Sonwalkar et al. (2009) report that the spectra of all types of WM echoes detected by RPI are sensitive to the presence of FAI, and that they manifest this sensitivity on plasmagrams by various amounts of spreading in travel time, varying from 5–10 ms for the most discrete cases to 40 ms and more for the most diffuse events. The spreading can be occasioned by propagation on multiple paths through irregular regions with cross-$\boldsymbol{B_0}$ scale sizes of the order of 1–10 km or by forward and backward scattering from irregularities with scale sizes of the order of 10–100 m. Scattering may involve changes in group velocity at the time of coupling between a predominantly electromagnetic wave and a quasi-electrostatic wave at an irregularity boundary. For convenience, MR- and SR-WM echoes have been further classified by Sonwalkar et al. (2009) as either discrete, multipath or diffuse according to the amount of travel time spreading.

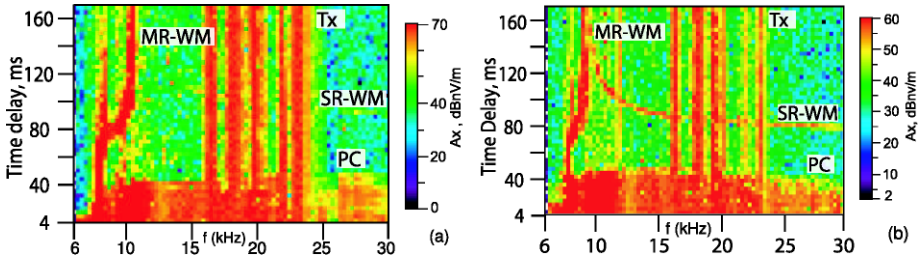

Fig. 18 (**a**) RPI plasmagram showing an MR-WM echo recorded on 23 October 2005 at 10:22:46 UT. Fixed frequency transmitter signals (Tx) are present, as well as a cluster of proton cyclotron (PC) echoes at delays <40 ms. (**b**) RPI record on 26 October 2005 at 09:32:42 UT with MR-WM echo and a well defined SR-SW echo, as well as Tx and PC echoes. (Adapted from Sonwalkar et al. 2009)

6.2 Examples of Magnetospherically Reflected and Specularly Reflected Whistler-Mode Echoes

Examples of MR- and SR-WM echoes are shown on RPI plasmagrams in Fig. 18. These records plot echo travel time in ms versus RPI transmitter frequency, which was stepped each 250 ms in 300 Hz increments from 6 to 63 kHz (only the range 6–30 kHz is displayed). In Fig. 18a, recorded at ∼2650 km and $L \approx 2.4$, a discrete MR-WM echo appears between ∼7.5 and ∼11 kHz. At ∼7.5 kHz the echo begins at the shortest delay displayed (∼4 ms) and extends with decreased amplitude to the top of the record. Beginning at a delay of ∼80 ms, the echo branches towards higher frequencies and extends to an undefined limiting delay at ∼11 kHz. Meanwhile, ground-based transmitter signals (Tx) appear between 16 and 23 kHz, extending over the full time-delay range available. Also present at frequencies above 8 kHz and at delays less than ∼40 ms is a band of proton cyclotron (PC) echoes (see Sect. 7), which are attributed to excitation of ambient protons in the antenna sheath by the leading edge of each 3.2-ms transmitter pulse (Carpenter et al. 2007).

Figure 18b, recorded at ∼2550 km and $L \approx 2.3$, also shows an MR-WM event, in this case with delimiting frequencies of ∼7 and ∼9 kHz. Transmitter signals are again present, although those near 16 and 23 kHz exhibit less spreading in frequency than those in Fig. 18a. A highlight of this record is a discrete SR-WM echo, which exhibits delays near 80 ms between ∼20 and 30 kHz but curves towards longer delays as it approaches the 9 kHz high frequency limit of the MR-WM echo.

Although examples of discrete, multipath, and diffuse SR-WM echoes were shown previously by Sonwalkar et al. (2004), RPI WM-echoes have now been observed much more extensively and categorized much more completely as a result of sounding operations at frequencies below 60 kHz in 2004 and 2005 (Sonwalkar et al. 2009).

6.3 Specularly Reflected Whistler-Mode Echoes

RPI soundings at WM frequencies regularly exhibit echoes that extend over a wide range of frequencies and are interpreted as having reflected from the steep density gradients at the bottom side of the ionosphere (Sonwalkar et al. 2004). Such SR-WM echoes often accompany MR-WM echoes, as illustrated by the example of Fig. 18b. Since an SR-WM echo provides an integral measure of the electron density between IMAGE, say at ∼3000 km, and the ionosphere at ∼100 km, it is particularly sensitive to density levels at altitudes below those reached by a simultaneous MR-WM event (∼1500 km). Thus its dispersion properties

may be used to constrain the density/plasma composition model that is found most consistent with the MR-WM event.

6.4 Magnetospherically Reflected Whistler-Mode Echoes and the Lower Hybrid Resonance

It may be seen in Fig. 12 that the Z-, O-, and X-mode dispersion diagrams each exhibit low frequency cutoffs, at which the refractive index goes to zero and the wave is reflected. That type of cutoff does not occur for WM waves. When the presence of ions is taken into account, the dispersion of WM is modified (not included in Fig. 12) such that WM waves, propagating at high wave normal angles with respect to $\boldsymbol{B_0}$ can undergo magnetospheric reflection at altitudes where $f \approx f_{lh}$. For an electron, H^+, He^+, and O^+ plasma, f_{lh} is given by the following equation:

$$\frac{1}{m_{\text{eff}}(m_p/m_e f_{lh}^2)} = \frac{1}{f_{pe}^2} + \frac{1}{f_{ce}^2}, \tag{2}$$

where m_p/m_e is the proton/electron mass ratio and the effective ion mass m_{eff} is defined as:

$$\frac{1}{m_{\text{eff}}} = \frac{\alpha}{1} + \frac{\beta}{4} + \frac{\gamma}{16}, \tag{3}$$

where α, β and γ are, respectively, the fractional abundances of H^+, He^+ and O^+.

The magnetospheric reflection is actually a refraction caused by a topological change and decrease in the size of the refractive index surface as the WM wave at large wave normal angle propagates from a region where $f_{lh} < f$ to a region where $f_{lh} > f$. When $f_{lh} < f$, the refractive index surface is "open", with a so called resonance cone (delimiting an angular region of no propagation), and when $f_{lh} > f$, it is "closed", such that the propagation is allowed at all angles with respect to $\boldsymbol{B_0}$ (Kimura 1966).

MR-WM echoes may exhibit a variety of discrete or diffuse spectral forms. MR-WM echoes with clearly identifiable forms, such as those illustrated in Fig. 18, tend to present a nose-like shape on plasmagrams because of extended time delays at the form's minimum and maximum frequencies. Those limiting frequencies, usually separated by a few kHz, are associated, respectively, with f_{lh} at the location of the satellite (the lower frequency), often near 6 kHz, and the maximum value of f_{lh} along the field line extending Earthward from IMAGE (the upper frequency), often in the range 9–12 kHz.

Key formative elements in the MR-WM echo phenomenon are believed to be: (i) propagation of RPI WM waves at high wave normal angles, near the so called resonance cone around the direction of the magnetic field; (ii) reflection of the waves near an altitude where the wave frequency is lower than but close to local f_{lh}; (iii) in the case of multipath or diffuse MR-WM echoes, refraction or scattering of the waves through encounters with FAI such that the echoes reach the satellite with varying time delays.

6.5 The Diagnostic Potential of Magnetospherically Reflected and Specularly Reflected Whistler-Mode Echoes

The time-delay-versus-frequency properties of MR-WM echoes provide a measure of f_{lh} along the field line passing through the satellite. The lower cutoff frequency of MR-WM echo, f_{lh} at the satellite, provides a measure of m_{eff} at that higher altitude where H^+ and He^+ may be dominant. The upper frequency cutoff of the MR-WM echo provides a measure

of the m_{eff} of the plasma in the important transition region (~1000–1500 km) between the O^+ dominated lower ionosphere and the H^+ dominated region at higher altitudes. This can be seen from expressions of (2) and (3) for f_{lh} and m_{eff}, respectively. It is clear that within altitude ranges over, which the r.h.s. of (2) does not change appreciably, the value of f_{lh} will be sensitive to changes in m_{eff} (by as much as a factor of 16) associated with altitude variations in ion composition.

Ray tracing simulations of the dispersion properties of simultaneously observed MR- and SR-WM echoes may be used for remote sensing of the ion composition and total electron density along a field line between the bottom of the ionosphere and the position of IMAGE (Sonwalkar et al. 2009). As noted, the MR-WM echo provides measures of the local m_{eff} and of m_{eff} at the altitude of the maximum f_{lh} below the satellite (in the vicinity of 1000 km). Meanwhile, the SR-WM echo, because of its noted sensitivity to the ionospheric electron density profile, provides an important constraint on the overall plasma density model used in the ray tracing simulation. Assuming a diffusive equilibrium model for magnetospheric density (see also Pierrard et al. 2009, this issue), Sonwalkar et al. (2009) developed a ray tracing method that determines the diffusive equilibrium model parameters such that the MR- and SR-WM dispersion and frequency cutoffs calculated from ray tracing simulations agree with those observed within experimental uncertainties. Applying this method in two specific instances, including the case shown in Fig. 18b, Sonwalkar et al. (2009) determined within 10% the electron and ion (H^+, He^+, O^+) densities along $\boldsymbol{B_0}$ ($L \approx 2$) passing through the satellite between 3000 km and 90 km.

7 Proton Cyclotron Echoes and a New Resonance

At altitudes ranging from ~1500 km to 20000 km in the plasmasphere, the RPI instrument onboard IMAGE can couple strongly to protons in the immediate vicinity of the satellite as it transmits 3.2-ms pulses and scans from 6 to 63 kHz or 20 to 326 kHz. Those soundings also give rise to a new resonance at a frequency ~15% above f_{ce} (Carpenter et al. 2007). The coupling to protons is revealed in echoes that arrive at multiples of the local proton gyroperiod t_p. Lower-altitude (<4000 km) versions of several of these proton cyclotron (PC) echo forms were observed in the topside ionosphere by sounders in the ISIS satellite era, among them discrete echoes in the WM domain below f_{ce} and in the nominally non-electromagnetically propagating domain above f_{ce} (e.g., Oya 1978; Horita 1987; Muldrew 1998). Also seen on ISIS satellites were spur-like broadenings of resonances such as the one at f_{pe} (e.g., King and Preece 1967; Benson 1975; Horita 1987).

7.1 The f_{ce}^+ Echo

Figure 19a shows an example of what has been called an f_{ce}^+ echo, a phenomenon often observed in the plasmasphere by RPI at frequencies from ~10 to 20% above f_{ce} (Carpenter et al. 2007). The plasmagram presents time delay from ~40 to 100 ms versus frequency from 20 to 50 kHz. IMAGE was at $L \approx 3.7$, well inside an extended plasmasphere at an altitude of ~14 000 km and in the mid-afternoon sector. The local electron density was ~560 cm^{-3}. The local value of f_{ce} is well defined at ~30 kHz by a resonance spike, a type of response that is regularly present on sounder records from the topside ionosphere (Benson 1977, and references cited therein). A band of WM noise extends upward in frequency to a relatively sharp cutoff at ~26 kHz. This band is attributed to multi-path propagation and scattering of a variety of WM signals, including naturally occurring wave emissions, WM emissions

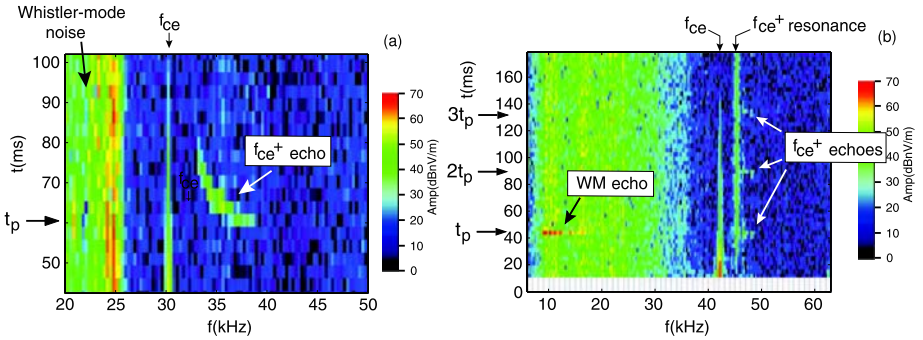

Fig. 19 (**a**) Portion of an RPI plasmagram showing a well defined proton cyclotron (PC) echo that exhibits extended delays at frequencies just above f_{ce} and then approaches a constant delay at the local value of the proton gyroperiod t_p. (**b**) RPI plasmagram illustrating three effects, a PC echo in the WM domain, a resonance at a frequency just above f_{ce}, and discrete echoes at multiples of t_p. (Adapted from Carpenter et al. 2007)

triggered by lightning, and multiple WM signals from ground-based transmitters. In the figure, the f_{ce}^{+} echo first appears at ~33 kHz, ~3 kHz above f_{ce}, and extends to 39 kHz. It exhibits a time-delay-versus-frequency form something like that of a hockey stick, at first falling steeply in delay with increasing frequency and then curving to reach a constant delay of ~61 ms. That delay corresponds closely to the local $t_p = 1836/f_{ce}$. On IMAGE the occurrence rates of PC echoes above f_{ce} were highest during periods when the angle ϕ between the spacecraft velocity vector and the geomagnetic field $\boldsymbol{B_0}$ was small, near 20°, but on occasion such echoes were detected when ϕ approached 90°.

7.2 The f_{ce}^{+} Resonance

A new phenomenon, called the f_{ce}^{+} resonance, has been observed at a frequency ~15% above f_{ce} (Carpenter et al. 2007). This resonance is apparently confined to altitudes above ~7000 km. It is illustrated by the plasmagram of Fig. 19b, which displays time delay from 0 to 178 ms versus frequency from 6 to 63 kHz. At the time of the figure, IMAGE was at $L \approx 3.6$ and at an altitude of ~12 000 km, well inside the plasmasphere. Three echo forms appear, a WM echo, multiple f_{ce}^{+} echoes, and an f_{ce}^{+} resonance. The WM echo, extending from ~9 to 17 kHz at a constant delay of ~45 ms, appears as a discrete intensity enhancement within the usual WM noise background. The value of f_{ce} is well marked by a tapered resonance spike at ~42 kHz. Approximately 3 kHz above f_{ce} is an f_{ce}^{+} resonance. This resonance differs from the spike at f_{ce} in that it extends to the top of the record and (in this case) is not clearly defined in the first ~30 ms after the beginning of the transmitter pulse. Along the high-frequency side of the f_{ce}^{+} resonance are f_{ce}^{+} echoes that arrived at multiples of t_p, the first at ~44.5 ms, the second at ~89 ms, and the third at ~133 ms. There are differences in amplitude among the echo forms illustrated in Fig. 19b: Portions of the WM echo near 10 kHz are ~10–15 dB stronger than the f_{ce}^{+} resonance or f_{ce}^{+} echoes.

7.3 Whistler-Mode Proton Cyclotron Echoes

Of special interest are exceptionally strong echoes in the WM domain near 10 kHz (Carpenter et al. 2007). On a given orbit, these invariably appeared at altitudes ~5000 km and below

and could be detected at altitudes up to ∼12 000 km. In some cases, the echoes appeared on plasmagrams showing other PC echo activity (see Fig. 19b). Most of the WM echoes observed thus far were found within the plasmasphere or the PBL, at *MLAT* between −60° and +60°. They were evident on occasion at higher latitudes and over the polar regions, but tended to be obscured there by strong natural WM noise with power spectral density 10 dB or more above the noise levels in the plasmasphere. Samplings showed strong WM echo activity at several widely spaced MLT, suggesting that such echoes may occur in all local time sectors.

At each frequency during a given sounding, WM echoes tended to repeat at time delays that were multiples of t_p. Figure 20 displays such effects on plasmagrams recorded on three different orbits at altitudes ∼10 700, ∼7700, and ∼4200 km, respectively. As altitude decreased, the inter-echo time delay decreased accordingly. In the stronger magnetic fields below ∼3000 km altitude, the time interval at each frequency between successive high-order echoes fell below 6.4 ms, the minimum interval allowing separation of echoes by one 3.2-ms time delay pixel, and individual echoes could no longer be resolved. In such cases, the echoes formed a "continuous" response extending to multiple values of t_p. When

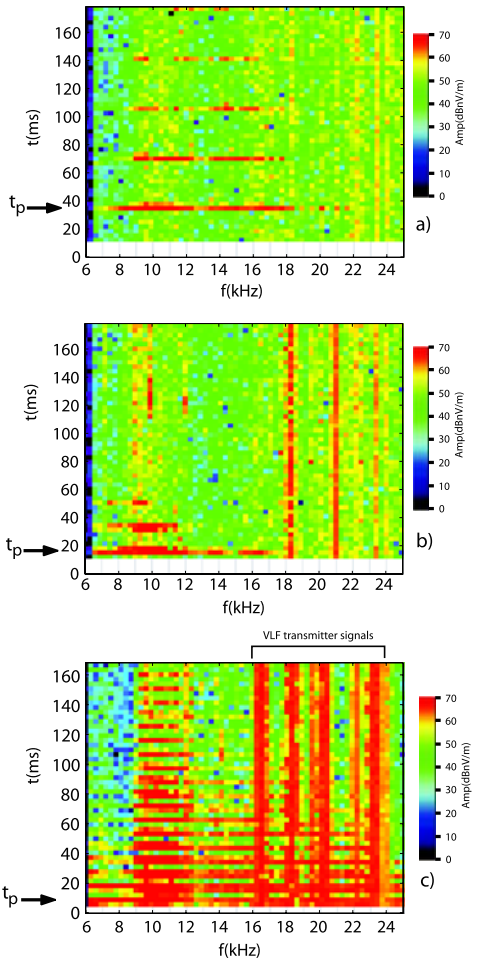

Fig. 20 RPI plasmagrams showing PC echoes in the WM domain, repeating at multiples of the local t_p. The examples were recorded on three different orbits at altitudes ∼10 700 km (**a**), ∼7700 km (**b**), and ∼4200 km (**c**). The *vertical lines* between 16 and 24 kHz in panel (**c**) represent WM transmissions from ground transmitters. (Adapted from Carpenter et al. 2007)

the angle ϕ was near a local minimum of order 10°, WM echoes were observed to repeat at multiples of t_p up to 15 or more. The data indicate that WM echo detection near 10 kHz was largely confined to a region of radius ∼300 m around the field line of excitation, and that the peak excitation of the protons occurred as a transient event at the beginning of each radio frequency (rf) pulse.

7.4 Comments on Physical Mechanisms of Proton Cyclotron Echoes

Carpenter et al. (2007) suggest that PC echoes and the new resonance are driven by a variety of mechanisms. Time delay measurements of WM echoes near 10 kHz indicated that the energization of the protons by a given 3.2-ms sounder pulse was essentially a transient process that occurred at the beginning of the pulse, and to that extent did not involve replication of the rf pulse by the echo. It was inferred that there is spatial bunching of accelerated protons during the initial formation of an electron sheath around the positive-voltage antenna element. The gyrating protons then produce a series of electrostatic pulses at multiples of t_p. Tight bunching of accelerated protons does not occur during the remainder of a 3.2-ms pulse, since ambient electrons never again appear close to the antenna during this period (due to the acceleration of protons during negative half cycles, protons near the antenna have a wide distribution of energies and thus are not subject to tight bunching during subsequent positive half cycles).

Most WM echoes were observed when IMAGE moved at low angles to $\boldsymbol{B_0}$ and was within a distance of ∼300 m transverse to the field line of original excitation of the plasma. The echoes showed no measurable WM propagation delay from a source, which is consistent with the inferred electrostatic nature of the echoes and the closeness of the antenna to the source field lines. The high intensity of the lower-order WM echoes, which regularly saturated the RPI receiver near 10 kHz, as well as the lack of detectable WM echo activity above 12 000 km altitude, were attributed in part to the fact that proton energization at the leading edge of the sounder pulse was at maximum levels when the rf of the pulse was below, but near, the local proton plasma frequency $f_{pp} = f_{pe}/43$. f_{pp} reaches a maximum of ∼13 kHz at the lower IMAGE altitudes, but falls below 6 kHz (the lowest sounder operating frequency) above 12 000 km.

In contrast to WM echoes, f_{ce}^{+} echoes occurred at frequencies well above f_{pp} and were thus outside the range where significant transient energization was expected. Also in contrast to WM echoes, f_{ce}^{+} echoes appeared to replicate the sounder pulse frequency and in so doing experienced large frequency-dependent increases in travel time as f_{ce} was approached from above. This dispersion as well as a year-to-year decrease in f_{ce}^{+} echo activity with increasing separation of the antenna from the "excited" field lines, is consistent with an explanation of f_{ce}^{+} echoes observed in the ISIS satellites in terms of thermal-mode propagation from a perturbed proton distribution (Muldrew 1998). A possible source of energy for the comparatively weak f_{ce}^{+} echoes is the quasi-static electric field that exists in the ion sheath that surrounds each antenna element in the immediate aftermath of an rf pulse, as discussed in Carpenter et al. (2007).

The new resonance above f_{ce} suggested the existence of a ringing phenomenon in the plasma that is unique to altitudes above ∼7000 km. The resonance mechanism appears to operate independently of the f_{ce}^{+} echo mechanism, although both phenomena were found within a similar range of frequencies above f_{ce}. The long enduring nature of the resonances, lasting at times for at least 300 ms, suggests that the perturbed plasma environment in which the ringing occurred was carried with the spacecraft a kilometer or more beyond the ∼300 m transverse distance within which the WM echoes were found. The collapse of the ion sheath

following an rf pulse may provide energy for the ringing process. This collapse may on occasion delay the onset of the detected resonance, in the manner proposed by Muldrew (1972), who argued that in the case of certain ionospheric resonances, the antenna sheath may temporarily exclude very short wavelength stimulated waves.

Previously suggested processes that were considered relevant to PC echoes above f_{ce} and to the new resonance include: (i) coupling between an excited Z-mode wave and longitudinal plasma waves (Benson 1975), (ii) accumulation of negative charge on an electric antenna during an rf pulse (Oya 1978), and (iii) Bernstein-mode propagation to an antenna from an excited proton population (Muldrew 1998).

8 Chorus

8.1 Observations of Whistler-Mode Chorus Emissions by CLUSTER

Whistler-mode (WM) chorus emissions are electromagnetic waves in a frequency range from a few hundreds of Hz to several kHz. Chorus was first observed on the ground (Storey 1953) but spacecraft observations in the Earth magnetosphere are also frequent. Chorus often contains many distinct short-duration wave packets, which change their frequency at time scales of a fraction of 1 s (see reviews by Sazhin and Hayakawa 1992; Omura et al. 1991). The generation mechanism of chorus is not yet well understood. It is most often accepted that chorus is generated by a nonlinear process (Nunn et al. 1997; Trakhtengerts 1999; Trakhtengerts et al. 2004), which involves the electron cyclotron resonance of WM waves with energetic electrons.

WM chorus emissions are receiving an increased attention in connection with the acceleration of energetic electrons in the radiation belts (e.g., Horne et al. 2005). Important new results on chorus has been obtained with wave and particle instruments onboard CLUSTER as well as with the DOUBLE STAR spacecraft, which routinely detects chorus emissions, and with the low altitude DEMETER spacecraft. This research provided us with tests of the existing theories of the chorus source mechanism and particle acceleration, and further motivated theoretical work. In the next two subsections we discuss results, which can have implications for plasmaspheric physics, i.e., results on position and size of the chorus source region and on propagation of chorus from its source region.

8.2 Position and Size of the Chorus Source Region

During the period of very close separation distances of the CLUSTER spacecraft (of the order of hundreds of km), very similar chorus emissions were observed in their generation region close to the magnetic equatorial plane at a radial distance of 4.4 R_E (Fig. 21). Both linear and rank correlation analysis have been used by Santolík and Gurnett (2003) and Santolík et al. (2004a) to define perpendicular dimensions of the sources of lower-band chorus elements below $\frac{1}{2} f_{ce}$. Correlation was significant in the range of separation distances of up to 260 km parallel to the field line and up to 100 km in the perpendicular plane. At these scales, the correlation coefficient was independent on parallel separations and decreased with perpendicular separation. This characteristic perpendicular scale varied between 60 and 200 km for different data intervals inside the source region. This variation was consistent with a simultaneously acting effect of random positions of locations at which the individual coherent wave packets of chorus were generated. The statistical properties of the observations were consistent with a model of the source region assuming individual sources of separate wave packets

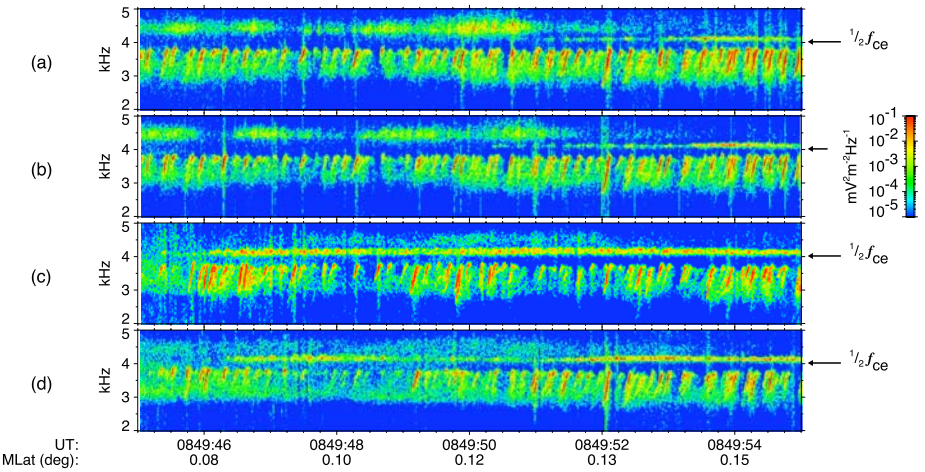

Fig. 21 Detailed time–frequency power spectrograms of electric field fluctuations in the source region recorded by the WBD instruments onboard the four CLUSTER spacecraft on 18 April 2002. Panels (**a**)–(**d**) show data from C1–C4, respectively. *Arrows* indicate local $\frac{1}{2} f_{ce}$ for each spacecraft. *MLAT* is given on the bottom for C1. Radial distance is 4.4 R_E, and MLT is 21:01 during this interval. (Adapted from Santolík and Gurnett 2003)

as Gaussian peaks of power radiated from individual active areas with a common half-width of 35 km perpendicular to the magnetic field (Santolík et al. 2004a). This characteristic scale was comparable to the wavelength of observed WM waves.

Central position of the source region from multipoint measurement of the Poynting flux is located close to the magnetic equatorial plane (Parrot et al. 2003; Santolík et al. 2003, 2004b, 2005a). Observed spatio-temporal variations of the direction of the Poynting flux consistently show that the central position of the chorus source fluctuates at time scales of minutes within a few thousands of km of the magnetic equator (Fig. 22). The typical order of magnitude of the speed of this motion is 100 $\mathrm{km\,s^{-1}}$. Note that this is a global speed of motion of the central position of the entire source region. It has been determined from the Poynting flux measurements where we always average propagation properties of several chorus wave packets. This speed is thus different from the speed of motion of individual sources discussed by Inan et al. (2004), Platino et al. (2006), Breneman et al. (2007) and Chum et al. (2007). Estimates of the electromagnetic planarity can be used to characterize the extent of the source in the direction parallel to the field line, obtaining at a radial distance of ∼4 R_E a source extent of 3000–5000 km (Santolík et al. 2004b, 2005a). This is consistent with theoretical results (Trakhtengerts et al. 2004) and with recent numerical simulations (Omura et al. 2008).

Santolík et al. (2005b) used the first measurements of the STAFF/DWP instrument on the DOUBLE STAR TC-1 spacecraft to investigate radial variation of intensity of WM chorus for L between 4 and 12. The chorus events showed an increased intensity at $L > 6$, consistent with intensifications of chorus, which were previously observed closer to the Earth at higher latitudes.

8.3 Propagation of Chorus From its Source Region

The four CLUSTER spacecraft observed that intense chorus waves propagate away from the equator simultaneously with lower-intensity waves propagating towards the equator (Parrot

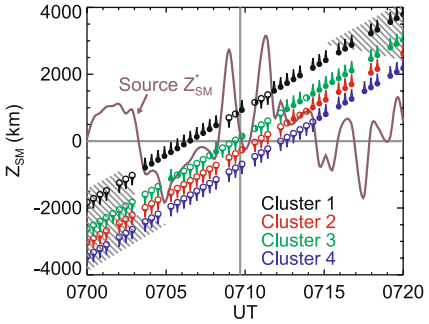

Fig. 22 Z_{SM} coordinate of the four CLUSTER spacecraft during the geomagnetic storm on 31 March 2001 as a function of time. Sign of the parallel component of the Poynting flux is shown by *downward arrows* attached to the *open symbols*, and by *upward arrows* with the *solid symbols*, for southward and northward components, respectively. The *half-filled symbols with no arrows* indicate that the sign cannot be reliably determined. *Horizontal grey line* is at the magnetic equator, *vertical grey line* shows the time when center of mass of the four spacecraft crosses the equatorial plane. *Shaded areas* bound the regions of low values of the electromagnetic planarity. *Purple line* shows the calculated position where the Poynting flux changes its sign. (Adapted from Santolík et al. 2004b)

et al. 2004a, 2004b). Using the observed wave normal directions of these waves, a backward ray tracing study predicts that the lower-intensity waves undergo the lower hybrid resonance (LHR) reflection at low altitudes (Parrot et al. 2004a). The rays of these waves then lead us back to their anticipated source region located close to the magnetic equator. This source region is, however, located at a different radial distance compared to the place of observation. The intensity ratio between magnetic component of the waves coming directly from the equator and waves returning to the equator has been observed between 0.005 and 0.01. The observations also show that waves returning to the equator after the magnetospherical reflection still have a high degree of polarization, even if they started to lose the coherent structure of the chorus elements (Parrot et al. 2004b).

Chum and Santolík (2005), Santolík et al. (2006) and Bortnik et al. (2007) showed that chorus can propagate to low altitudes towards the Earth if it is generated with Earthward inclined wave vectors. This result can be used to explain observations of low-altitude electromagnetic ELF hiss at subauroral latitudes. Santolík et al. (2006) reported observations of a divergent propagation pattern of these waves: They propagate with downward directed wave vectors, which are slightly equatorward inclined at lower *MLAT* and slightly poleward inclined at higher latitudes. Reverse ray tracing using different plasma density models indicated a possible source region near the magnetic equator at a radial distance between 5 and 7 R_E by a mechanism acting on highly oblique wave vectors. Additionally, waveforms received at altitudes of 700–1200 km by FREJA and DEMETER showed that low-altitude ELF hiss contains discrete time–frequency structures resembling wave packets of WM chorus. Detailed measurements of the CLUSTER spacecraft gave the time–frequency structure and frequencies of chorus along the reverse raypaths of ELF hiss, which are consistent with the hypothesis that the ELF hiss is a low-altitude manifestation of WM chorus. This propagation pattern applies mainly to the most frequently occurring dawn and dayside chorus. As noted in the following section these waves can also be considered as a possible additional candidate for the embryonic source of plasmaspheric hiss.

9 Hiss

The last comprehensive review on plasmaspheric and mid-latitude hiss was done by Hayakawa and Sazhin (1992). The following two sections are not an update to that work, but rather tries to put into context recent advances obtained on these natural waves thanks to the CLUSTER and IMAGE satellites.

9.1 Plasmaspheric Hiss

Plasmaspheric hiss is an electromagnetic emission confined to the plasmasphere. It occurs at all local times but is more intense on the dayside, and further intensifies with geomagnetic activity (Dunckel and Helliwell 1969; Russell et al. 1969; Thorne et al. 1973). Its spectral characteristics are similar to audible hiss: structureless and banded in frequency between ∼100 Hz and several kHz. Statistically, its intensity peaks near 500 Hz and is one order of magnitude more intense below than above 1 kHz (Fig. 23).

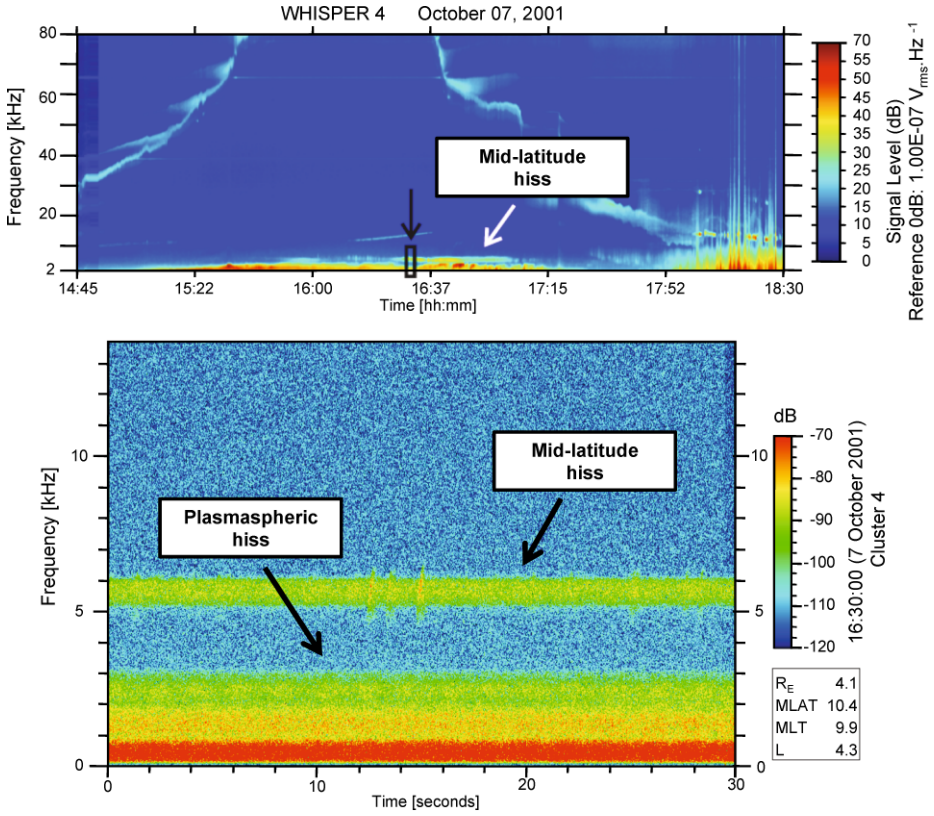

Fig. 23 (*Top*) WHISPER electric field spectrogram from C4 on 7 October 2001, from 14:45 to 18:30 UT. A banded hiss emission is observed from 16:25 to 17:04 UT (*white arrow*). The *black box* (*black arrow*) symbolizes the time period and the frequency range of the enlargement displayed in the *bottom panel*. (*Bottom*) High-time resolution WBD electric field spectrogram measured by C4 on 7 October 2001, during 30 s from 16:00:00.024 UT. The mid-latitude hiss emission is observed just above 5 kHz, while plasmaspheric hiss is observed from 100 Hz to 3 kHz with maximum spectral intensity below 700 Hz. (Adapted from Masson et al. 2004)

Plasmaspheric hiss has been studied since the late 1960s using observations from various satellites flying across the plasmasphere (Hayakawa and Sazhin 1992). It was found in particular that this emission plays a key role in the precipitation of relativistic electrons from the plasmasphere into the atmosphere (Sect. 9.1.1). However, even four decades after its discovery, its source location and generation mechanism remain controversial topics. As shown in Sect. 9.1.2, significant progresses have been made in recent years on these issues, thanks to data collected by several satellites including CLUSTER and IMAGE.

9.1.1 Impact on the Radiation Belts

The Van Allen radiation belts are two roughly concentric belts of energetic particles (>100 keV) encircling the Earth. The inner belt is characterized by a fairly stable population of high-energy protons (∼10–100 MeV), trapped between $L = 1.25$ and $L = 2$. The outer belt encircles the inner belt ($3 < L < 7$) and is characterized by a population of relativistic electrons (>1 MeV) and various ions (∼10 keV–10 MeV). However, the content of the outer belt fluctuates widely with regards to the geomagnetic activity. Between the inner and the outer belts ($2 < L < 3$), the population of relativistic electrons drops down by a factor of 10 to 100 (e.g., Brautigam et al. 2004). However, during very strong geomagnetic storms, this slot region can be filled with energetic particles. The slot region subsequently reforms on a timescale of days to weeks.

Theoretical work by Kennel and Petschek (1966) showed that natural waves propagating in the whistler mode are able to gain energy from a gyroresonance interaction with radiation belt relativistic electrons near the magnetic equator, causing them to change pitch angle and precipitate. Several types of WM waves exist in the plasmasphere (e.g., Green et al. 2005a) but plasmaspheric hiss was shown to be the dominant emission responsible for the electron scattering in the slot region (Lyons et al. 1972; Thorne et al. 1973; Abel and Thorne 1998). Plasmaspheric hiss was also found to be an important loss mechanism inside plasmaspheric plumes (Summers et al. 2008), the outer radiation belt (Meredith et al. 2007) and the upper part of the inner belt (Tsurutani et al. 1975) during magnetically disturbed periods.

Therefore understanding the origin of plasmaspheric hiss is of fundamental importance to forecast the distribution of relativistic electrons and dynamics of the radiation belts electrons.

9.1.2 Origin of Plasmaspheric Hiss

Over the years, two theories have emerged as the most likely candidates to explain the origin of plasmaspheric hiss. One of them considers the in situ growth and amplification of background electromagnetic turbulence in space, driven by unstable energetic electron populations (Thorne et al. 1973). Unfortunately, typical wave growth rates estimated in the plasmasphere are too weak to locally generate the hiss emissions with its observed power. However, once hiss is generated, its power can be maintained thanks to the presence of these anisotropic energetic electrons in the outer plasmasphere, via a physical process known as cyclotron resonant instability (Church and Thorne 1983).

The other theory considers terrestrial lightning strikes as the main energy source of plasmaspheric hiss (Dowden 1971; Sonwalkar and Inan 1989; Draganov et al. 1993; Bortnik et al. 2003). Lightning strikes trigger the emission of impulsive signals that can reach the plasmasphere. As they propagate, they undergo dispersion as lower frequencies travel slower than higher ones, sounding like a whistler when turned to audio. Several of these lightning-generated whistlers can finally merge into a broadband signal that becomes plasmaspheric hiss as originally suggested by H.C. Koons according to Storey et al. (1991).

Using a new statistical wave-mapping technique on data collected by DE-1 and IMAGE, Green et al. (2005a) showed that the distribution of hiss emissions in the plasmasphere at 3 kHz is similar to the geographic distribution of lightning strikes. In particular, the observed emissions are stronger over the continents than the oceans. The 3 kHz frequency was chosen since it is the lowest frequency of the IMAGE/RPI instrument. They claim that geographic control of a portion of the hiss spectrum exists to some extent above ∼500 Hz, although the DE/PWI data below 1.2 kHz were only examined in a qualitative manner (Green et al. 2006). They concluded that lightning is the dominant source of plasmaspheric hiss. But this conclusion has been called into question by Thorne et al. (2006) arguing in particular that the intensities of the waves above 1 kHz are much smaller than the intensities of plasmaspheric hiss below 1 kHz.

Meredith et al. (2006) subsequently analyzed the geographic distribution of hiss over a wider frequency range (0.1–5.0 kHz) using CRRES data. They found that the waves between 1.0 kHz and 5.0 kHz are most likely related to lightning-generated whistlers, confirming the results obtained by Green et al. (2005a) at 3 kHz. However, they found that the waves at lower frequencies (0.1–1.0 kHz) are independent of lightning activity. Since the emission power of plasmaspheric hiss below 1 kHz is statistically an order of magnitude higher than above 1 kHz, lightning strikes are not responsible for the bulk of the wave power of plasmaspheric hiss. As electron loss via pitch angle scattering is proportional to the wave power, this suggests that lightning strikes is not the dominant energy source, which maintains the slot region in the radiation belts during quiet to moderate geomagnetic activity. In other words, both leading models for the origin of plasmaspheric hiss are not fully backed up by observations.

An alternative explanation for the generation of plasmaspheric hiss was proposed by Chum and Santolík (2005) who discovered that chorus, a well-known intense electromagnetic emission generated outside the plasmasphere, can fill the plasmasphere and might be one of the possible sources of plasmaspheric hiss (see Sect. 8). They also found that the wave-normal angles of these waves stay far from resonance and therefore effects of Landau damping can be excluded. Additionally the wave normals are nearly field-aligned inside the plasmasphere, consistent with previous observations of plasmaspheric hiss. This makes possible further amplification of these waves by the cyclotron resonance (e.g., Santolík et al. 2001). Equatorward reflected ELF hiss at low altitudes that is also most probably related to chorus emissions might represent another simultaneously acting embryonic source (Santolík et al. 2006). The results of Chum and Santolík (2005) were reproduced and confirmed by Bortnik et al. (2008) who obtained the same effect and who verified the absence of Landau damping. According to this study, plasmaspheric hiss is driven by chorus emissions. By modeling the propagation of chorus to lower altitudes, Bortnik et al. (2008) are able to reproduce the main features of plasmaspheric hiss including its observed spectral signature, incoherent nature and day-night asymmetry in intensity.

9.2 Mid-Latitude Hiss

9.2.1 Mid-Latitude Hiss and Auroral Hiss

Mid-latitude hiss (MLH) emissions are natural radio waves that usually appear as a band-limited white noise with a central frequency contained between 2 and 10 kHz and a spectral bandwidth of 1 to 2 kHz (Fig. 23). Such hiss emissions were first discovered by ground-based observatories located at mid-latitudes (30–60°) in the 1950s and 1960s (Watts 1957; Laaspere et al. 1964; Helliwell 1965). When converted to audio range, these VLF waves (3–30 kHz) have a characteristic “hissing” sound, hence their name.

The first studies of this natural phenomenon suggested that they were just auroral hiss, sometimes called polar hiss (Ondoh 2006), propagating from auroral latitudes to mid-latitudes within the Earth-ionosphere waveguide. This was shown to be incorrect in the pioneering works by Harang (1968) and Hayakawa et al. (1975). Significant differences between auroral and MLH spectral signatures were found between simultaneous measurements from stations located at mid- (34.5°) and auroral (69°) latitudes (see Hayakawa and Sazhin 1992, for the last comprehensive review on MLH). In particular, the upper limit of MLH spectrum could extend up to 8 kHz while the auroral hiss spectrum could extend up to 500 kHz or even higher.

Since then, hiss events recorded at mid- or even low-latitude stations have been considered to be independent from auroral hiss. Mid- and low- latitude hisses are both named MLH since the maximum of their occurrence was found at middle latitudes, 55° to 65° (Helliwell 1965). This latitudinal range is magnetically connected to the plasmapause location, which explains why MLH is sometimes called narrow-band plasmapause hiss or simply plasmapause hiss (e.g., Ondoh 2006).

Thanks to satellite measurements and theoretical studies, other fundamental differences have been discovered between auroral and MLH, such as their source location and generation mechanism.

9.2.2 Source Location and Generation Mechanism

Ground-based direction finding performed by Hayakawa et al. (1986) revealed that MLH is generated mainly on the inner side of the PBL. For the first time, a survey of MLH events observed close to their source region by the CLUSTER satellites confirmed the presence of MLH around the magnetic equator, in the PBL at around 4 R_E, i.e., 25 000 km altitude (Masson et al. 2004).

MLH, like chorus, is generated near the magnetic equator and propagate via the whistler mode. Chorus often accompanies MLH and the upper cutoff of the combined band of hiss and chorus is found to be proportional to the equatorial gyrofrequency (Dunckel and Helliwell 1969). Both type of waves are believed to be generated by the electron cyclotron instability, sometimes called the whistler-mode instability. Combined ground-based and satellite measurements reveal that mid-latitude/plasmapause hiss waves are excited around the equatorial plasmapause by the cyclotron instability of electrons with energy of a few keV convected from the magnetotail (e.g., Hayakawa and Sazhin 1992; Ondoh 2006, and references therein).

Unlike MLH, auroral hiss emissions are broad, intense electromagnetic emissions, which occur over a wide frequency range from a few hundred Hz to several tens of kHz. At low frequencies, auroral hiss occurs in a narrow latitudinal band, typically only 5–10° wide, centered on the auroral zone (70–80°). At high frequencies, the emission spreads out over a broad region, both towards the polar cap, and to a lesser extent towards the equator. The anisotropic character of whistler-mode propagation causes this spreading at high frequencies.

Satellite data, such as those from POLAR, also revealed that auroral hiss is emitted in a beam around an auroral magnetic field line located between $L = 2$ and $L = 4$. Downward propagating auroral hiss emissions are closely correlated with intense, downgoing 100 eV to 40 keV electron beams precipitating from the plasmasheet boundary layer in geomagnetic quiet and disturbed periods (Gurnett and Franck 1972). Upward propagating auroral hiss is correlated with upgoing ∼50 eV electron beams.

All these facts confirm ground-based initial measurements: Auroral hiss and MLH are two distinct natural phenomena.

9.2.3 Geomagnetic Activity Impact

Several physical characteristics of MLH are affected by geomagnetic activity, starting with their duration. During quiet geomagnetic conditions, such a band-limited white noise usually lasts for an hour. However, during active periods, MLH can last for several hours showing amplitude fluctuations on a time scale of tens of minutes (see page 427 of Sonwalkar 1995).

According to Ondoh (2006), the occurrence rate of MLH is maximum under geomagnetic quiet conditions (30 nT $< AE <$ 200 nT) while the occurrence rate of auroral/polar hiss is much larger in the substorm period (200 nT $< AE <$ 924 nT). This statistical study is based on 65 MLH and 74 polar hisses observed by the ISIS-2 satellite (1400 km altitude, polar circular orbit) under various geomagnetic conditions.

Close to the source region, in the vicinity of the magnetic equator at 4 R_E, Masson et al. (2004) showed that the central frequency of MLH (f_0) is correlated with the K_p index: the higher K_p, the higher f_0. One possible explanation suggested in this paper assumes that these waves are generated in the vicinity of the plasmapause, near the magnetic equator, in a given f/f_{ce} frequency bandwidth. At the equator near the plasmapause f_{ce} is proportional to $1/L_{pp}^3$, where L_{pp} is the geocentric radial distance of the plasmapause. When geomagnetic activity is high, the plasmasphere is compressed, the plasmapause location gets closer to the Earth, and so L_{pp} decreases. In this case, f_{ce} will increase, hence f_0 increases too, according to our assumption (f_0/f_{ce} constant). This explanation is in agreement with theoretical predictions (Sazhin 1989; Hayakawa and Sazhin 1992) and with early ground-based measurements, which revealed that the central frequency of hiss usually increases with decreasing latitude (Laaspere et al. 1964). This behaviour is similar to plasmaspheric hiss, whose wave frequencies just inside the plasmapause increase with increasing K_p (Thorne et al. 1973).

10 Equatorial Noise

10.1 Introduction

Emissions called "equatorial noise" are electromagnetic waves (the term "fast magnetosonic waves" is also sometimes used, e.g., Horne et al. 2000 2007) observed close to the magnetic equator (within $\sim \pm 3°$) at frequencies between f_{ce} and f_{lh} and at radial distances $R = 2$–$7\ R_E$. They propagate in the fast magnetosonic mode coupled to the whistler mode with wave vectors nearly perpendicular to the ambient magnetic field ($\boldsymbol{B_0}$), with magnetic field fluctuations linearly polarized in the direction of $\boldsymbol{B_0}$. Electric field fluctuations are elliptically polarized with a low ellipticity (from 0.02 to 0.11, see Santolík et al. 2002), major polarization axis being oriented along the wave vector. CLUSTER observes emissions of this type during perigee passes through the equatorial region ($R \approx 4\ R_E$).

Figure 24 shows an example of equatorial noise emissions recorded by C4 on 17 February 2002 within approximately $\pm 30°$ of magnetic equator. Panels (**a**) and (**b**) represent frequency–time spectrograms of power-spectral densities of the magnetic and electric field fluctuations, respectively. Equatorial noise is the intense electromagnetic emission seen on both panels close to the center of the time interval, within a few degrees from the magnetic equator. In the frequency domain it appears as two main peaks at about 30 Hz and 70 Hz. The emission is confined below the upper estimate of f_{lh}, calculated as the geometric average of the proton gyrofrequency f_{cp} and f_{ce} (solid line at ~300 Hz). Frequency–time spectrogram of ellipticity of polarization of the magnetic field fluctuations is shown

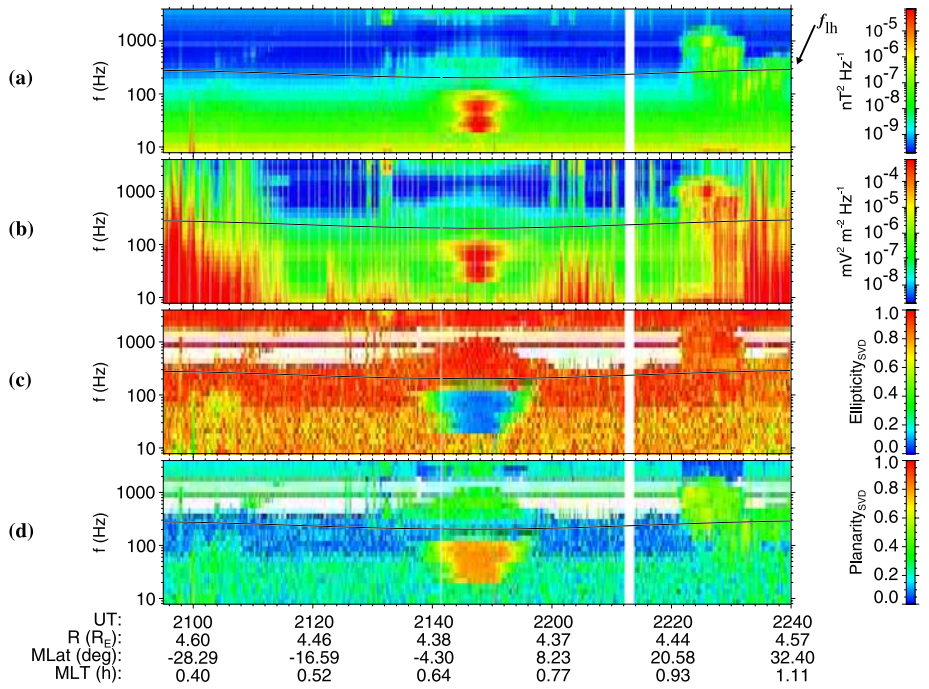

Fig. 24 STAFF data collected by C4 on 17 February 2002: (**a**) sum of the power-spectral densities of the three magnetic components, (**b**) sum of the power-spectral densities of the two electric components, (**c**) ellipticity and (**d**) planarity determined using the singular value decomposition of the magnetic spectral matrix. Maximum possible value of f_{lh} is plotted over the panels (**a**)–(**d**). The data in panels (**c**) and (**d**) are not shown for weak signals below 10^{-9} nT^2 Hz^{-1}. (Adapted from Santolík et al. 2004c)

in panel (**c**). It varies between 0 (linear polarization) and 1 (circular polarization). Equatorial noise can be easily distinguished by its polarization close to linear, as it was first described by Russell et al. (1970). Panel (**d**) represents the frequency–time spectrogram of planarity of magnetic field fluctuations. A value close to 1 represents a strict confinement of the magnetic field fluctuations to a single plane, which is obviously also true for the linear polarization.

10.2 CLUSTER Observations

Santolík et al. (2002) performed a multipoint case study of equatorial noise by using both STAFF and WBD instruments onboard CLUSTER. Frequency–time spectrograms of the analyzed electric field data measured by WBD instruments are shown in Fig. 25. Dipole equator and min-B equator calculated from a Tsyganenko-IGRF model (which is about 1° northward from the dipole equator) are marked. It can be seen that what appears like a noise in a low resolution data is in fact a set of many spectral lines (Gurnett 1976) some of which follow a harmonic pattern. However, all the possible fundamental frequencies were significantly different from the local f_{cp} and they did not match the cyclotron frequencies of heavier ions either. The authors bring observational evidence that the waves propagate with a significant radial component (on average the waves propagate at ∼45° between the radial and azimuthal directions, but the wave power spreads in a large angular interval) and can thus propagate

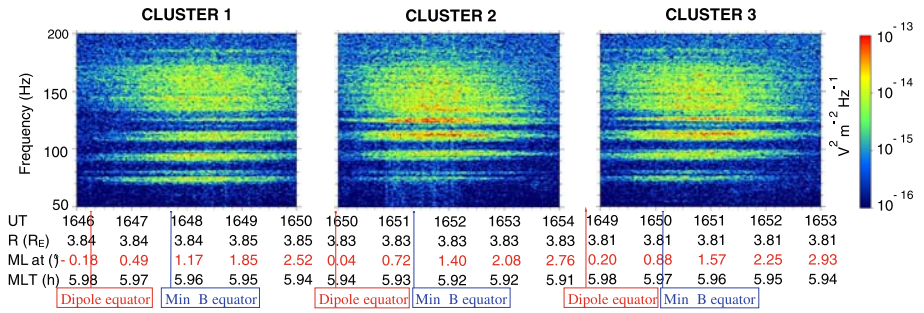

Fig. 25 Frequency–time spectrograms of electric field data recorded by the WBD instrument onboard three CLUSTER spacecraft on 4 December 2000. (Adapted from Santolík et al. 2002)

from a distant generation region located at different radial distances where ion cyclotron frequencies match the observed fine structure.

Santolík et al. (2004c) performed a systematic analysis of 2 years of STAFF data measured by CLUSTER during their perigee passes through equatorial region. A visual inspection has revealed the presence of equatorial noise in 398 of the 671 analyzed passes (each spacecraft has been treated separately), which corresponds to about 59%. They have selected 16 frequency channels between 8 Hz (the lowest frequency analyzed by the STAFF instrument) and 300 Hz (the upper estimate of the maximum f_{lh} throughout the dataset) and with the time resolution of 4 s evaluated the wave parameters within $\pm 30°$ of geomagnetic latitude (altogether, about 1.4×10^7 frequency–time intervals). They have shown that a value of 0.2 is a reasonable upper estimate of the ellipticity of magnetic field fluctuations of equatorial noise and that equatorial noise has the largest power spectral density of magnetic field fluctuations among all the natural emissions in the given interval of frequencies and latitudes.

Němec et al. (2005) have used the same dataset, but limited to only $\pm 10°$ of geomagnetic latitude. Following Santolík et al. (2004c) they selected the 16 lowest frequency bands and only the frequency–time intervals during which the ellipticity was lower than 0.2. Then they calculated average power-spectral density from the selected data in the selected frequency channels and found parameters λ_c (central latitude) and Δ (full width at half of maximum, FWHM) of a Gaussian model of the power-spectral density as a function of geomagnetic latitude. The resulting parameters were found to be about the same for magnetic and electric power spectral densities. Most of the central latitudes occur within 2° from the magnetic equator with the FWHM lower than 3°. From the original frequency-dependent data, they calculated a time-averaged spectral matrix over the time interval where the spacecraft was located inside the latitudinal interval from $\lambda_c - \Delta$ to $\lambda_c + \Delta$ and obtained the probability density of frequencies of equatorial noise emissions normalized to the local f_{cp}. It has been shown that the most probable frequency of emissions is between 4 and 5 local f_{cp}, with probability density slowly decreasing towards the higher frequencies. Finally, multipoint measurements performed by CLUSTER were used to demonstrate that variations of the ratio of amplitudes of equatorial noise increase with time delay between measurements in an interval from tenths to hundreds of minutes, but these variations do not seem to increase with separations up to 0.7 R_E in the equatorial plane.

Němec et al. (2006) performed the similar analysis, but used an improved magnetic field model to determine the min-B equator (instead of a dipole magnetic field model used in the previous study). They concluded that central latitudes of equatorial noise seem to be

located exactly at the true magnetic equator and that the observed deviations can be most probably explained by the inaccuracies in the model. They also used cold plasma theory to calculate the number density from the ratio of magnetic and electric power spectral density. The estimated values vary from units to hundreds of particles per cubic centimeter and are in a rough agreement with the densities obtained from the measurements of the spacecraft potential.

10.3 Generation Mechanism of Equatorial Noise and its Effects

A generation mechanism of equatorial noise (fast magnetosonic waves) is discussed by Horne et al. (2000). They conducted a ray-tracing analysis using a density model, which includes a plasmasphere, a plasmapause, and a radial variation in the plasma density outside the plasmasphere, as well as the proton distribution with a thermal spread of velocities taken from spacecraft observations, and a realistic plasma sheet electron distribution to represent conditions outside the plasmapause. Supposing ring distribution functions (ring velocity v_R) with a thermal spread of velocities, they showed that magnetosonic waves can be generated just outside the plasmapause and propagate well inside the plasmapause without substantial absorption. Peak growth occurs for very large angles of propagation, and thus the waves are confined in latitude to a few degrees about the magnetic equator. The instability analysis shows that a good "rule of thumb" for growth of magnetosonic waves at large angles of propagation ($\sim$89°) is $v_R > v_A$ for growth $f > 30 f_{cp}$, and $v_R > 2v_A$ for growth $f < 30 f_{cp}$ (f is the frequency of wave, v_A is the Alfvén speed).

In a recent paper Horne et al. (2007) discussed potential implications of fast magnetosonic waves for electron populations in Van Allen radiation belts and demonstrated that the fast magnetosonic waves can accelerate electrons between $\sim$10 keV and a few MeV inside the outer radiation belt. The acceleration occurs via the Landau resonance, and not Doppler shifted cyclotron resonance, due to the wave propagation almost perpendicular to the ambient magnetic field. Pitch angle and energy diffusion rates are comparable to those obtained for WM chorus. This suggests that the magnetosonic waves are very important for local electron acceleration and could play an important role in the process of energy transfer from the ring current (where ion ring distributions are formed during magnetic storms as a result of losses due to slow ion drift) to Van Allen radiation belts. Finally, since magnetosonic waves do not scatter electrons into the loss cone, the need for a continuous supply of low energy electrons is not as stringent as it is for their acceleration by chorus, and these waves, on their own, are not important for loss to the atmosphere.

11 ULF Resonances

11.1 Historical Description

The attempt to use pulsation data to remotely sense plasmaspheric mass properties has a long history (Troitskaya and Gul'Elmi 1969; Lanzerotti and Fukunishi 1975; Webb et al. 1977; Takahashi and McPherron 1982). A variety of methods have been developed to identify inner magnetospheric field line resonances, which can arise from a driving impulse. These include complex demodulation (Webb 1979), methods of evaluating the spectral matrix (Arthur 1979), such as state vector analysis techniques (Samson 1983), meridional geomagnetic gradient evaluation (Baransky et al. 1985), cross phase analysis techniques (Waters et al. 1991), and dynamic spectrum techniques (Menk 1988). It is not always easy to determine the resonant frequencies because the pulsation spectrum can be dominated by the source mechanism

(Kurchashov et al. 1987). The "gradient method" was developed by Baransky et al. (1985) to separate the mixed driving and resonant power. Field line resonant theory predicts that the wave power peaks at the resonant frequency and the spatial profile of the phase at the resonant frequency changes roughly 180 degrees across the resonant L-shell (Tamao 1964; Chen and Hasegawa 1974; Southwood 1974). Using data from two magnetometers located on the same magnetic longitude and closely separated in latitude, one can compare the wave phase or amplitude seen at both stations and obtain the eigenfrequencies of the field line midway between the two stations. The cross phase spectral technique developed by Waters et al. (1991) was used by Menk et al. (1994, 1999) to monitor the temporal evolution of plasmaspheric properties. This is done by identifying the maximum interstation phase difference between two closely spaced stations (few hundred km) to identify the eigenfrequencies of the local field line. With this diagnostic technique variations in plasmaspheric plasma parameters (such as equatorial plasma density) can be monitored and using a latitudinal array of stations, the location of the plasmapause can be determined. The techniques of Schulz (1996) and Denton and Gallagher (2000) are used to derive the equatorial mass density from the inferred eigenfrequency of the field line (Berube et al. 2003). The techniques are analogous to identifying the mass of a string by determining the sound frequency of the plucked note. By knowing the string length (field line length), string tension (strength of magnetic field line) and the frequency of oscillation, the density of the string (plasma) can be inferred. Under the usual Alfvénic travel time approximations, the eigenfrequencies can be expressed as:

$$\frac{\omega_n}{2\pi} \approx \frac{n\Delta\omega}{2\pi} \approx n\left(\int \frac{ds}{v_A}\right)^{-1}, \tag{4}$$

where v_A is the Alfvén speed, n is the harmonic number, and s is the coordinate that measures the arc length of the field line. The measure eigenfrequency is representative of the equatorial mass density because of the slow Alfvén speed there. The ability to uniquely identify the flux tubes eigenfrequency depends on having a solar wind or magnetospheric driving wave. On the dayside of the Earth, ULF waves are almost continuously present due to upstream waves impinging on the magnetopause (e.g., Yumoto 1986). These driver waves excite the field lines resonance frequency that can be separated out from the driving frequency using such methods as the cross phase technique. Therefore one limitation of using ULF waves at the present time is that inner magnetospheric mass densities can only be routinely measured during the daytime.

Figure 26 shows daily plasma mass density averages inferred from ULF resonances during 2000–2001 at $L = 1.74$. The daily averages are made from hourly estimates of the eigenfrequency. The error bars shown are representative of the variation of the mean of the hourly estimates. The December densities are 2–3 times higher than the June densities for both years. Typical uncertainties in determining the ULF resonant frequency, and hence mass density is $\pm 25\%$ (e.g., Berube et al. 2003, 2005). Annual variation of the electron density has also been observed at low latitudes using VLF measurements (e.g., Clilverd et al. 1991).

11.2 IMAGE Observations

The mass density of the inner plasmasphere is difficult to measure and the few satellites capable of making measurements did not sample the inner magnetosphere well. An exception are measurements from DE-1 (e.g., Horwitz et al. 1984). Most studies found that the relative abundances of heavy ions in the plasmasphere vary greatly. Craven et al. (1997) using data

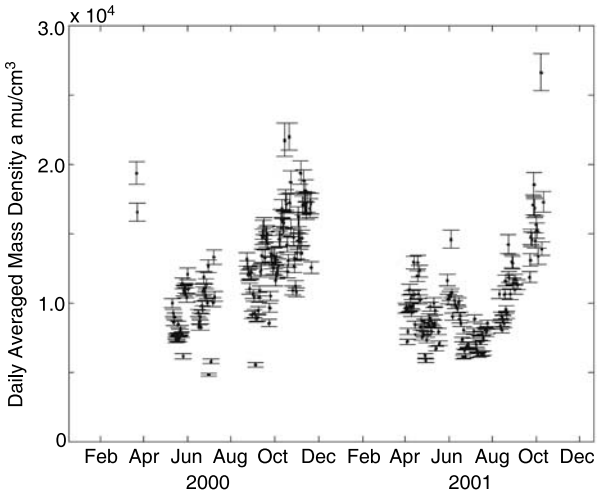

Fig. 26 The equatorial mass densities at $L = 1.74$ computed by a ULF resonance method. Note the seasonal difference in mass density. (Adapted from Berube et al. 2003)

from DE-1 found He^+ to H^+ ratios in the plasmasphere of ∼0.03–0.3, implying He^+ abundances of ∼3–23 percent by number, assuming no other heavy ions are present. Horwitz et al. (1984) found that in the aftermath of a storm, O^+ density could become comparable to H^+ density in the plasmasphere. The first empirical model of the equatorial mass density of the plasmasphere was proposed by Berube et al. (2005) using ground-based ULF wave diagnostics. Plasmaspheric mass density between $L = 1.7$ and $L = 3.2$ was determined using over 5200 hours of data from pairs of stations in the MEASURE array of ground magnetometers. The least squares fit to the data as a function of L shows that mass density falls logarithmically with L. Average ion mass as a function of L was also estimated by combining the mass density model with plasmaspheric electron density profiles determined from IMAGE/RPI instrument. Additionally, the RPI electron density database was used to examine how the average ion mass changes under different levels of geomagnetic activity. Berube et al. (2005) report that average ion mass is greatest under the most disturbed conditions. This result indicates that heavy ion concentrations (percent by number) are enhanced during large geomagnetic disturbances. The average ion mass was also found to increase with increasing L (below 3.2), indicating the presence of a heavy ion torus during disturbed times. Heavy ions must play an important role in storm-time plasmaspheric dynamics. The average ion mass was also used to constrain the concentrations of He^+ and O^+. Estimates of the He^+ concentration determined this way is useful for interpreting IMAGE/EUV images. More details on empirical models can be found elsewhere in this issue (Reinisch et al. 2009).

12 Conclusion

CLUSTER and IMAGE are pioneer space missions with regards to plasmaspheric wave phenomena thanks to their new experimental capabilities. Some of the results highlighted in this paper were considered among the science objectives of these missions such as the source location of waves (Sects. 3 and 8) or the remote sensing of density profiles along geomagnetic field lines (Sect. 5). Now, CLUSTER and IMAGE have also brought or led to a wealth of unforeseen results, just like pioneer missions do.

For instance, the database of plasmaspheric density profiles measured by IMAGE, together with ground-based ULF wave diagnostics, has helped determining the average ion

mass as a function of L under different levels of geomagnetic activity. Thanks to a better knowledge of this key physical parameter, heavy ions were found to play an important role in storm-time plasmaspheric dynamics (Sect. 11).

Similarly, the IMAGE/EUV imager uncovered the presence of density bite-outs of the plasmapause named notches. Together with local wave observations, these EUV images have enabled to identify these notches as the source of kilometric continuum (KC); recall that KC is the high-frequency range of a more general wave phenomenon known as the non-thermal continuum (NTC) radiation. As KC emission cone is constrained by the geometry of these density cavities, KC observations provide back information on this plasmaspheric structure and its dynamics (Sect. 3).

Such a link between density irregularities in azimuth and longitudinal beaming properties of radiations is likely applicable to NTC radiations at lower frequency, linking them with irregularities of smaller size (Sect. 4). CLUSTER observations in the NTC range have also revealed a new class of radio sources, emitting from the mid-latitude plasmapause boundary while new radio echoes have been discovered by IMAGE (Sects. 6 and 7).

Another striking example concerns chorus emissions. The multipoint view of CLUSTER near perigee has enabled a better understanding of the source location and size of these waves and their propagation properties from their source region (Sect. 8). This new knowledge has triggered ray-tracing studies that led to an unforeseen conclusion: Chorus is an embryonic source of plasmaspheric hiss, the dominant emission responsible for the scattering of MeV electrons in the electron slot region (Sect. 9).

As usual, scientific discoveries lead to more questions than answers. For instance, CLUSTER data strongly suggest that equatorial noise plays, like chorus, a role in the acceleration of electrons in the outskirts of the plasmasphere (Sect. 10). However, a crucial limitation of this conclusion lies in the limited range of radial distances of equatorial perigee passes (3.9–5 R_E). A full assessment of the importance of these waves requires detailed analysis of the occurrence rate of their power as a function of L, MLT and latitude.

Overall, both missions have helped to better relate plasmaspheric wave phenomena with plasmaspheric density structures, derive electron density profiles and heavy particles content of the plasmasphere, better locate the source of waves and how they propagate. They have also increased our knowledge on how electrons of magnetotail origin are accelerated up to MeV range and how these killer electrons get scattered by waves. Last but not least, these missions have linked wave phenomena together: Several waves are now considered as embryonic sources of other waves and no more studied as distinct phenomena. In other words, IMAGE and CLUSTER have helped putting the puzzle pieces together.

But the puzzle is far from being complete. Upcoming inner magnetospheric missions will all orbit the magnetic equator and carry appropriate wave instrumentation. These missions are the NASA's Radiation Belt Storm Probes (RBSP) composed of two satellites (launch planned in 2012), the ERG (Energization and Radiation in Geospace) single satellite project from Japan and the ORBITALS (Outer Radiation Belt Injection, Transport, Acceleration and Loss Satellite) project led by Canada. Up till the launch of RBSP and hopefully ERG and ORBITALS, three of the NASA's THEMIS spacecraft launched in 2007 and equipped with search coil magnetometers will survey the inner magnetosphere together with particle instrumentation. In other words, the future looks bright for plasmaspheric wave research.

Acknowledgements O. Santolík and F. Němec acknowledge grants GAAV A301120601 and ME842. F. Darrouzet acknowledges the support by the Belgian Federal Science Policy Office (BELSPO) through the ESA/PRODEX project (contract 13127/98/NL/VJ (IC)). This paper is an outcome of the workshop "The Earth's plasmasphere: A CLUSTER, IMAGE, and modeling perspective", organized by the Belgian Institute for Space Aeronomy in Brussels in September 2007. Figures 1, 2, 4, 8, 10b, 11, 13, 14, 15, 16, 17, 18, 19,

20, 21, 22, 25, 26: Copyright (1999, 2002 and 2004, 2002, 2008, 1991, 2008, 2003, 2003, 2003, 2003, 2003, 2009, 2007, 2007, 2003, 2004, 2002, 2003), with permission from American Geophysical Union (AGU). Figure 10a: Copyright (1982), with permission from Elsevier. Figures 10c, 23, 24: Copyright (2007, 2004, 2004), with permission from European Geosciences Union (EGU). Figure 12: Copyright (1995), with permission from Cambridge University Press.

References

B. Abel, R.M. Thorne, Electron scattering loss in Earth's inner magnetosphere 1. Dominant physical processes. J. Geophys. Res. **103**(A2), 2385–2396 (1998)

C.W. Arthur, Digital techniques for ULF wave polarization analysis. Ann. Telecommun. **34**, 166–178 (1979)

L.N. Baransky, J.E. Borovkov, M.B. Gokhberg, S.M. Krylov, V.A. Troitskaya, High resolution method of direct measurement of the magnetic field lines' eigen frequencies. Planet. Space Sci. **33**(12), 1369–1374 (1985)

R.F. Benson, Ion effects on ionospheric electron resonance phenomena. Radio Sci. **10**(2), 173–185 (1975)

R.F. Benson, Stimulated plasma waves in the ionosphere. Radio Sci. **12**(6), 861–878 (1977)

R.F. Benson, Elusive upper hybrid waves in the auroral topside ionosphere, in *Auroral Plasma Dynamics*, ed. by R.L. Lysak. Geophysical Monograph Series, vol. 80 (American Geophysical Union, Washington, 1993), pp. 267–274

R.F. Benson, H.K. Wong, Low-altitude ISIS 1 observations of auroral radio emissions and their significance to the cyclotron maser instability. J. Geophys. Res. **92**(A2), 1218–1230 (1987)

R.F. Benson, V.A. Osherovich, J. Fainberg, B.W. Reinisch, Classification of IMAGE/RPI-stimulated plasma resonances for the accurate determination of magnetospheric electron density and magnetic field values. J. Geophys. Res. **108**(A5), 1207 (2003)

R.F. Benson, P.A. Webb, J.L. Green, D.L. Carpenter, V.S. Sonwalkar, H.G. James, B.W. Reinisch, Active wave experiments in space plasmas: The Z mode, in *Geospace Electromagnetic Waves and Radiation*, ed. by J.W. LaBelle, R.A. Treumann. Lecture Notes in Physics, vol. 687 (Springer, Berlin, 2006), pp. 3–36

D. Berube, M.B. Moldwin, J.M. Weygand, An automated method for the detection of field line resonance frequencies using ground magnetometer techniques. J. Geophys. Res. **108**(A9), 1348 (2003)

D. Berube, M.B. Moldwin, S.F. Fung, J.L. Green, A plasmaspheric mass density model and constraints on its heavy ion concentration. J. Geophys. Res. **110**, A04212 (2005)

J. Bortnik, U.S. Inan, T.F. Bell, Frequency-time spectra of magnetospherically reflecting whistlers in the plasmasphere. J. Geophys. Res. **108**(A1), 1030 (2003)

J. Bortnik, R.M. Thorne, N.P. Meredith, O. Santolík, Ray tracing of penetrating chorus and its implications for the radiation belts. Geophys. Res. Lett. **34**, L15109 (2007)

J. Bortnik, R.M. Thorne, N.P. Meredith, The unexpected origin of plasmaspheric hiss from discrete chorus emissions. Nature **452**(7183), 62–66 (2008)

D.H. Brautigam, K.P. Ray, G.P. Ginet, D. Madden, Specification of the radiation belt slot region: Comparison of the NASA AE8 model with TSX5/CEASE data. IEEE Trans. Nucl. Sci. **51**(6), 3375–3380 (2004)

A. Breneman, C.A. Kletzing, J. Chum, O. Santolík, D. Gurnett, J. Pickett, Multispacecraft observations of chorus dispersion and source location. J. Geophys. Res. **112**, A05221 (2007)

J.L. Burch, IMAGE mission overview. Space Sci. Rev. **91**(1–2), 1–14 (2000)

W. Calvert, Oblique z-mode echoes in the topside ionosphere. J. Geophys. Res. **71**(23), 5579–5583 (1966)

P. Canu, P.M.E. Décréau, S. Escoffier, S. Grimald, Observations of continuum radiations close to the plasmapause: Evidence for small scale sources, in *Planetary Radio Emissions VI*, ed. by H.O. Rucker, W.S. Kurth, G. Mann (Austrian Academy of Sciences Press, Vienna, 2006)

D.L. Carpenter, R.R. Anderson, An ISEE/Whistler model of equatorial electron density in the magnetosphere. J. Geophys. Res. **97**(A2), 1097–1108 (1992)

D.L. Carpenter, J. Lemaire, The plasmasphere boundary layer. Ann. Geophys. **22**(12), 4291–4298 (2004)

D.L. Carpenter, R.R. Anderson, W. Calvert, M.B. Moldwin, CRRES observations of density cavities inside the plasmasphere. J. Geophys. Res. **105**(A10), 23323–23338 (2000)

D.L. Carpenter, T.F. Bell, U.S. Inan, R.F. Benson, V.S. Sonwalkar, B.W. Reinisch, D.L. Gallagher, Z-mode sounding within propagation "cavities" and other inner magnetospheric regions by the RPI instrument on the IMAGE satellite. J. Geophys. Res. **108**(A12), 1421 (2003)

D.L. Carpenter, T.F. Bell, D. Chen, D. Ng, C. Baran, B.W. Reinisch, I. Galkin, Proton cyclotron echoes and a new resonance observed by the Radio Plasma Imager instrument on the IMAGE satellite. J. Geophys. Res. **112**, A08208 (2007)

L. Chen, A. Hasegawa, A theory of long-period magnetic pulsations, 1. Steady state excitation of field line resonance. J. Geophys. Res. **79**(7), 1024–1032 (1974)

J. Chum, O. Santolík, Propagation of whistler-mode chorus to low altitudes: divergent ray trajectories and ground accessibility. Ann. Geophys. **23**(12), 3727–3738 (2005)

J. Chum, O. Santolík, A.W. Breneman, C.A. Kletzing, D.A. Gurnett, J.S. Pickett, Chorus source properties that produce time shifts and frequency range differences observed on different Cluster spacecraft. J. Geophys. Res. **112**, A06206 (2007)

S.R. Church, R.M. Thorne, On the origin of plasmaspheric hiss: Ray path integrated amplification. J. Geophys. Res. **88**(A10), 7941–7957 (1983)

M.A. Clilverd, A.J. Smith, N.R. Thomson, The annual variation in quiet time plasmaspheric electron density, determined from whistler mode group delays. Planet. Space Sci. **39**(7), 1059–1067 (1991)

N. Cornilleau-Wehrlin, G. Chanteur, S. Perraut, L. Rezeau, P. Robert, A. Roux, C. de Villedary, P. Canu, M. Maksimovic, Y. de Conchy, D. Hubert, C. Lacombe, F. Lefeuvre, M. Parrot, J.L. Pinçon, P.M.E. Décréau, C.C. Harvey, P. Louarn, O. Santolík, H.S.C. Alleyne, M. Roth, T. Chust, O. Le Contel, STAFF team, First results obtained by the Cluster STAFF experiment. Ann. Geophys. **21**(1–2), 437–456 (2003)

P.D. Craven, D.L. Gallagher, R.H. Comfort, Relative concentration of He^+ in the inner magnetosphere as observed by the DE 1 retarding ions mass spectrometer. J. Geophys. Res. **102**(A2), 2279–2289 (1997)

F. Darrouzet, J. De Keyser, P.M.E. Décréau, J.F. Lemaire, M.W. Dunlop, Spatial gradients in the plasmasphere from Cluster. Geophys. Res. Lett. **33**, L08105 (2006)

F. Darrouzet, D.L. Gallagher, N. André, D.L. Carpenter, I. Dandouras, P.M.E. Décréau, J. De Keyser, R.E. Denton, J.C. Foster, J. Goldstein, M.B. Moldwin, B.W. Reinisch, B.R. Sandel, J. Tu, Plasmaspheric density structures and dynamics: Properties observed by the CLUSTER and IMAGE missions. Space Sci. Rev. (2009, this issue)

J. De Keyser, D.L. Carpenter, F. Darrouzet, D.L. Gallagher, J. Tu, CLUSTER and IMAGE: New ways to study the Earth's plasmasphere. Space Sci. Rev. (2009, this issue)

P.M.E. Décréau, P. Fergeau, V. Krasnosels'kikh, E. Le Guirriec, M. Lévêque, P. Martin, O. Randriamboarison, J.L. Rauch, F.X. Sené, H.C. Séran, J.G. Trotignon, P. Canu, N. Cornilleau, H. de Féraudy, H. Alleyne, K. Yearby, P.B. Mögensen, G. Gustafsson, M. André, D.A. Gurnett, F. Darrouzet, J. Lemaire, C.C. Harvey, P. Travnicek, Whisper experimenters, Early results from the Whisper instrument on Cluster: an overview. Ann. Geophys. **19**(10–12), 1241–1258 (2001)

P.M.E. Décréau, C. Ducoin, G. Le Rouzic, O. Randriamboarison, J.L. Rauch, X. Trotignon, J.G. Vallières, P. Canu, F. Darrouzet, M.P. Gough, A. Buckley, T.D. Carozzi, Observation of Continuum radiations from the CLUSTER fleet: first results from direction finding. Ann. Geophys. **22**(7), 2607–2624 (2004)

R.E. Denton, D.L. Gallagher, Determining the mass density along magnetic field lines from toroidal eigenfrequencies. J. Geophys. Res. **105**(A12), 27717–27725 (2000)

R.L. Dowden, Distinction between mid latitude VLF hiss and discrete emissions. Planet. Space Sci. **19**(3), 374–376 (1971)

A.B. Draganov, U.S. Inan, V.S. Sonwalkar, T.F. Bell, Whistlers and plasmaspheric hiss: Wave directions and three-dimensional propagation. J. Geophys. Res. **98**(A7), 11401–11410 (1993)

N. Dunckel, R.A. Helliwell, Whistler-mode emissions on the OGO 1 satellite. J. Geophys. Res. **74**(26), 6371–6385 (1969)

F. El-Lemdani Mazouz, J.L. Rauch, P.M.E. Décréau, J.G. Trotignon, X. Vallières, F. Darrouzet, P. Canu, X. Suraud, Wave emissions at half electron gyroharmonics in the equatorial plasmasphere region: CLUSTER observations and statistics. Adv. Space Res. **43**(2), 253–264 (2009)

C.P. Escoubet, C.T. Russell, R. Schmidt (eds.), *The Cluster and Phoenix Missions* (Kluwer, Dordrecht, 1997)

W.M. Farrell, Direct generation of O-mode emission in a dense, warm plasma: Applications to interplanetary type II emissions and others in its class. J. Geophys. Res. **106**(A8), 15701–15709 (2001)

S.F. Fung, R.F. Benson, D.L. Carpenter, J.L. Green, V. Jayanti, I.A. Galkin, B.W. Reinisch, Guided echoes in the magnetosphere: Observations by Radio Plasma Imager on IMAGE. Geophys. Res. Lett. **30**(11), 1589 (2003)

G.K. Goertz, R.J. Strangeway, Plasma waves, in *Introduction to Space Physics*, ed. by M.G. Kivelson, C.T. Russell (Cambridge University Press, Cambridge, 1995), pp. 356–399

M.P. Gough, Non-thermal continuum emissions associated with electron injections: Remote plasmapause sounding. Planet. Space Sci. **30**(7), 657–668 (1982)

J.L. Green, S.A. Boardsen, Confinement of nonthermal continuum radiation to low latitudes. J. Geophys. Res. **104**(A5), 10307–10316 (1999)

J.L. Green, S.F. Fung, Advances in inner magnetosphere passive and active wave research, in *The Inner Magnetosphere: Physics and Modeling*, ed. by T.I. Pulkkinen, N.A. Tsyganenko, R.H.W. Friedel. Geophysical Monograph Series, vol. 155 (American Geophysical Union, Washington, 2005), pp. 181–202

J.L. Green, B.R. Sandel, S.F. Fung, D.L. Gallagher, B.W. Reinisch, On the origin of kilometric continuum. J. Geophys. Res. **107**(A7), 1105 (2002)
J.L. Green, S. Boardsen, S.F. Fung, H. Matsumoto, K. Hashimoto, R.R. Anderson, B.R. Sandel, B.W. Reinisch, Association of kilometric continuum radiation with plasmaspheric structures. J. Geophys. Res. **109**, A03203 (2004)
J.L. Green, S. Boardsen, L. Garcia, W.W.L. Taylor, S.F. Fung, B.W. Reinisch, On the origin of whistler mode radiation in the plasmasphere. J. Geophys. Res. **110**, A03201 (2005a)
J.L. Green, S.F. Fung, S. Boardsen, H.J. Christian, Distribution and origin of plasmapsheric plasma waves, in *Inner Magnetosphere Interactions: New Perspectives from Imaging*, ed. by J. Burch, M. Schulz, H. Spence. Geophysical Monograph Series, vol. 159 (American Geophysical Union, Washington, 2005b), pp. 113–126
J.L. Green, S. Boardsen, L. Garcia, S.F. Fung, B.W. Reinisch, Reply to "Comment on "On the origin of whistler mode radiation in the plasmasphere" by Green et al." J. Geophys. Res. **111**, A09211 (2006)
S. Grimald, Etude de l'émission et de la propagation du continuum terrestre à partir des données des satellites Cluster. Ph.D. thesis, University of Orléans, France, 2007
S. Grimald, P.M.E. Décréau, P. Canu, X. Suraud, X. Vallières, F. Darrouzet, C.C. Harvey, A quantitative test of Jones NTC beaming theory using CLUSTER constellation. Ann. Geophys. **25**(3), 823–831 (2007)
S. Grimald, P.M.E. Décréau, P. Canu, A. Rochel, X. Vallières, Medium-latitude sources of plasmaspheric non-thermal continuum radiations observed close to harmonics of the electron gyrofrequency. J. Geophys. Res. **113**, A11216 (2008)
D.A. Gurnett, The Earth as a radio source: The nonthermal continuum. J. Geophys. Res. **80**(19), 2751–2763 (1975)
D.A. Gurnett, Plasma wave interactions with energetic ions near the magnetic equator. J. Geophys. Res. **81**(16), 2765–2770 (1976)
D.A. Gurnett, L.A. Franck, VLF hiss and related plasma observations in the polar magnetosphere. J. Geophys. Res. **77**(1), 172–190 (1972)
D.A. Gurnett, S.D. Shawhan, R.R. Shaw, Auroral hiss, Z mode radiation, and auroral kilometric radiation in the polar magnetosphere: DE 1 observations. J. Geophys. Res. **88**(A1), 329–340 (1983)
D.A. Gurnett, R.L. Huff, J.S. Pickett, A.M. Persoon, R.L. Mutel, I.W. Christopher, C.A. Kletzing, U.S. Inan, W.L. Martin, J.-L. Bougeret, H.S.C. Alleyne, K.H. Yearby, First results from the Cluster wideband plasma wave investigation. Ann. Geophys. **19**(10–12), 1259–1272 (2001)
G. Gustafsson, M. André, T. Carozzi, A.I. Eriksson, C.-G. Fälthammar, R. Grard, G. Holmgren, J.A. Holtet, N. Ivchenko, T. Karlsson, Y. Khotyaintsev, S. Klimov, H. Laakso, P.-A. Lindqvist, B. Lybekk, G. Marklund, F. Mozer, K. Mursula, A. Pedersen, B. Popielawska, S. Savin, K. Stasiewicz, P. Tanskanen, A. Vaivads, J.-E. Wahlund, First results of electric field and density observations by Cluster EFW based on initial months of observations. Ann. Geophys. **19**(10–12), 1219–1240 (2001)
L. Harang, VLF-emissions observed at stations close to the auroral zone at stations on lower latitudes. J. Atmos. Terr. Phys. **30**, 1143–1160 (1968)
K. Hashimoto, W. Calvert, H. Matsumoto, Kilometric continuum detected by Geotail. J. Geophys. Res. **104**(A12), 28645–28656 (1999)
M. Hayakawa, S.S. Sazhin, Mid-latitude and plasmaspheric hiss: A review. Planet. Space Sci. **40**(10), 1325–1338 (1992)
M. Hayakawa, Y. Tanaka, J. Ohtsu, The morphologies of low-latitude and auroral VLF "hiss". J. Atmos. Terr. Phys. **37**, 517–529 (1975)
M. Hayakawa, N. Ohmi, M. Parrot, F. Lefeuvre, Direction finding of ELF hiss emissions in a detached plasma region of the magnetosphere. J. Geophys. Res. **91**(A1), 135–141 (1986)
R.A. Helliwell, *Whistlers and Associated Ionospheric Phenomena* (Stanford University Press, Stanford, 1965)
R.E. Horita, Proton cyclotron echoes and spurs observed on Alouette II and ISIS II. Radio Sci. **22**(4), 671–686 (1987)
R.B. Horne, G.V. Wheeler, H.S.C.K. Alleyne, Proton and electron heating by radially propagating fast magnetosonic waves. J. Geophys. Res. **105**(A12), 27597–27610 (2000)
R.B. Horne, R.M. Thorne, Y.Y. Shprits, N.P. Meredith, S.A. Glauert, A.J. Smith, S.G. Kanekal, D.N. Baker, M.J. Engebretson, J.L. Posch, M. Spasojevic, U.S. Inan, J.S. Pickett, P.M.E. Décréau, Wave acceleration of electrons in the Van Allen radiation belts. Nature **437**(7056), 227–230 (2005)
R.B. Horne, R.M. Thorne, S.A. Glauert, N.P. Meredith, D. Pokhotelov, O. Santolík, Electron acceleration in the Van Allen radiation belts by fast magnetosonic waves. Geophys. Res. Lett. **34**, L17107 (2007)
J.L. Horwitz, R.H. Comfort, C.R. Chappell, Thermal ion composition measurements of the formation of the new outer plasmasphere and double plasmapause during storm recovery phase. Geophys. Res. Lett. **11**(8), 701–704 (1984)

X. Huang, B.W. Reinisch, P. Song, J.L. Green, D.L. Gallagher, Developing an empirical density model of the plasmasphere using IMAGE/RPI observations. Adv. Space Res. **33**(6), 829–832 (2004)
U.S. Inan, M. Platino, T.F. Bell, D.A. Gurnett, J.S. Pickett, Cluster measurements of rapidly moving sources of ELF/VLF chorus. J. Geophys. Res. **109**, A05214 (2004)
J.E. Jackson, The reduction of topside ionograms to electron-density profiles. Proc. IEEE **57**(6), 960–975 (1969)
H.G. James, Wave propagation experiments at medium frequencies between two ionospheric satellites, 3. Z mode pulses. J. Geophys. Res. **84**(A2), 499–506 (1979)
D. Jones, Latitudinal beaming of planetary radio emissions. Nature **288**, 225–229 (1980)
D. Jones, Terrestrial myriametric radiation from the Earth's plasmapause. Planet. Space Sci. **30**(4), 399–410 (1982)
Y. Kasaba, H. Matsumoto, K. Hashimoto, R.R. Anderson, J.-L. Bougeret, M.L. Kaiser, X.Y. Wu, I. Nagano, Remote sensing of the plasmapause during substorms: Geotail observation of nonthermal continuum enhancement. J. Geophys. Res. **103**(A9), 20389–20405 (1998)
C.F. Kennel, H.E. Petschek, Limit on stably trapped particle fluxes. J. Geophys. Res. **71**(1), 1–28 (1966)
I. Kimura, Effects of ions on whistler-mode ray tracing. Radio Sci. **1**(3), 269–283 (1966)
J.W. King, D.M. Preece, Observations of proton gyroeffects in the topside ionosphere. J. Atmos. Terr. Phys. **29**, 1387–1390 (1967)
I.P. Kurchashov, I.S. Nikomarov, V.A. Pilipenko, A. Best, Field line resonance effects in local meridional structure of mid-latitude geomagnetic pulsations. Ann. Geophys. **5**(6), 147–154 (1987)
W.S. Kurth, Detailed observations of the source of terrestrial narrowband electromagnetic radiation. Geophys. Res. Lett. **9**(12), 1341–1344 (1982)
W.S. Kurth, D.A. Gurnett, R.R. Anderson, Escaping nonthermal continuum radiation. J. Geophys. Res. **86**(A7), 5519–5531 (1981)
T. Laaspere, M.G. Morgan, W.C. Johnson, Chorus, hiss, and other audio-frequency emissions at stations of the whistlers-east network. Proc. IEEE **52**(11), 1331–1349 (1964)
J. LaBelle, R.A. Treumann, Auroral radio emissions, 1. Hisses, roars, and bursts. Space Sci. Rev. **101**(3), 295–440 (2002)
L.J. Lanzerotti, H. Fukunishi, Relationships of the characteristics of magnetohydrodynamic waves to plasma density gradients in the vicinity of the plasmapause. J. Geophys. Res. **80**(34), 4627–4634 (1975)
J.F. Lemaire, K.I. Gringauz, *The Earth's Plasmasphere* (Cambridge University Press, New York, 1998)
B.T. Loftus, T.E. Van Zandt, W. Calvert, Observations of conjugate ducting by the fixed-frequency topside-sounder satellite. Ann. Geophys. **22**(4), 530–537 (1966)
L.R. Lyons, R.M. Thorne, C.F. Kennel, Pitch-angle diffusion of radiation belt electrons within the plasmasphere. J. Geophys. Res. **77**(19), 3455–3474 (1972)
A. Masson, U.S. Inan, H. Laakso, O. Santolík, P. Décréau, Cluster observations of mid-latitude hiss near the plasmapause. Ann. Geophys. **22**(7), 2565–2575 (2004)
H. Matsui, J.C. Foster, D.L. Carpenter, I. Dandouras, F. Darrouzet, J. De Keyser, D.L. Gallagher, J. Goldstein, P.A. Puhl-Quinn, C. Vallat, Electric fields and magnetic fields in the plasmasphere: A perspective from CLUSTER and IMAGE. Space Sci. Rev. (2009, this issue)
C.E. McIlwain, Coordinates for mapping the distribution of magnetically trapped particles. J. Geophys. Res. **66**(11), 3681–3691 (1961)
F.W. Menk, Spectral structure of mid-latitude Pc3-4 geomagnetic pulsations. J. Geomagn. Geoelectr. **40**(1), 33–61 (1988)
F.W. Menk, B.J. Fraser, C.L. Waters, C.W.S. Ziesolleck, Q. Feng, S.H. Lee, P.W. McNabb, Ground measurements of low latitude magnetospheric field line resonances, in *Solar Wind Sources of Magnetospheric Ultra-Low-Frequency Waves*, ed. by M.J. Engebretson, K. Takahashi, M. Scholer. Geophysical Monograph Series, vol. 81 (American Geophysical Union, Washington, 1994), pp. 299–310
F.W. Menk, D. Orr, M.A. Clilverd, A.J. Smith, C.L. Waters, D.K. Milling, B.J. Fraser, Monitoring spatial and temporal variations in the dayside plasmasphere using geomagnetic field line resonances. J. Geophys. Res. **104**(A9), 19955–19969 (1999)
N.P. Meredith, R.B. Horne, M.A. Clilverd, D. Horsfall, R.M. Thorne, R.R. Anderson, Origins of plasmaspheric hiss. J. Geophys. Res. **111**, A09217 (2006)
N.P. Meredith, R.B. Horne, S.A. Glauert, R.R. Anderson, Slot region electron loss timescales due to plasmaspheric hiss and lightning-generated whistlers. J. Geophys. Res. **112**, A08214 (2007)
D.D. Morgan, D.A. Gurnett, The source location and beaming of terrestrial continuum radiation. J. Geophys. Res. **96**(A6), 9595–9613 (1991)
D.B. Muldrew, Radio propagation along magnetic field-aligned sheets of ionization observed by the Alouette topside sounder. J. Geophys. Res. **68**(19), 5355–5370 (1963)
D.B. Muldrew, Nonvertical propagation and delayed-echo generation observed by the topside sounders. Proc. IEEE **57**(6), 1097–1107 (1969)

D.B. Muldrew, Electrostatic resonances associated with the maximum frequencies of cyclotron-harmonic waves. J. Geophys. Res. **77**(10), 1794–1801 (1972)
D.B. Muldrew, Topside sounder proton-cyclotron echo generation from a plasma memory process and electron Bernstein-wave propagation. Radio Sci. **33**(5), 1395–1411 (1998)
F. Němec, O. Santolík, K. Gereová, E. Macúšová, Y. de Conchy, N. Cornilleau-Wehrlin, Initial results of a survey of equatorial noise emissions observed by the Cluster spacecraft. Planet. Space Sci. **53**(1–3), 291–298 (2005)
F. Němec, O. Santolík, K. Gereová, E. Macúšová, H. Laakso, Y. de Conchy, M. Maksimovic, N. Cornilleau-Wehrlin, Equatorial noise: Statistical study of its localization and the derived number density. Adv. Space Res. **37**(3), 610–616 (2006)
D. Nunn, Y. Omura, H. Matsumoto, I. Nagano, S. Yagitani, The numerical simulation of VLF chorus and discrete emissions observed on the Geotail satellite using a Vlasov code. J. Geophys. Res. **102**(A12), 27083–27097 (1997)
Y. Omura, H. Matsumoto, D. Nunn, M.J. Rycroft, A review of observational, theoretical and numerical studies of VLF triggered emissions. J. Atmos. Terr. Phys. **53**(5), 351–368 (1991)
Y. Omura, Y. Katoh, D. Summers, Theory and simulation of the generation of whistler-mode chorus. J. Geophys. Res. **113**, A04223 (2008)
T. Ondoh, Latitudinal changes of polar hiss and plasmapause hiss associated with magnetospheric processes. Adv. Space Res. **37**(3), 581–591 (2006)
H. Oya, Generation mechanism of proton cyclotron echoes due to pulsed radio frequency waves in space plasma. J. Geophys. Res. **83**(A5), 1991–2008 (1978)
M. Parrot, O. Santolík, N. Cornilleau-Wehrlin, M. Maksimovic, C.C. Harvey, Source location of chorus emissions observed by Cluster. Ann. Geophys. **22**(2), 473–480 (2003)
M. Parrot, O. Santolík, N. Cornilleau-Wehrlin, M. Maksimovic, C. Harvey, Magnetospherically reflected chorus waves revealed by ray tracing with CLUSTER data. Ann. Geophys. **21**(5), 1111–1120 (2004a)
M. Parrot, O. Santolík, D.A. Gurnett, J.S. Pickett, N. Cornilleau-Wehrlin, Characteristics of magnetospherically reflected chorus waves observed by CLUSTER. Ann. Geophys. **22**(7), 2597–2606 (2004b)
V. Pierrard, J. Goldstein, N. André, V.K. Jordanova, G.A. Kotova, J.F. Lemaire, M.W. Liemohn, H. Matsui, Recent progress in physics-based models of the plasmasphere. Space Sci. Rev. (2009, this issue)
M. Platino, U.S. Inan, T.F. Bell, J.S. Pickett, P. Canu, Rapidly moving sources of upper band ELF/VLF chorus near the magnetic equator. J. Geophys. Res. **111**, A09218 (2006)
B.W. Reinisch, D.M. Haines, K. Bibl, G. Cheney, I.A. Galkin, X. Huang, S.H. Myers, G.S. Sales, R.F. Benson, S.F. Fung, J.L. Green, S. Boardsen, W.W.L. Taylor, J.-L. Bougeret, R. Manning, N. Meyer-Vernet, M. Moncuquet, D.L. Carpenter, D.L. Gallagher, P. Reiff, The Radio Plasma Imager investigation on the IMAGE spacecraft. Space Sci. Rev. **91**(1–2), 319–359 (2000)
B.W. Reinisch, X. Huang, D.M. Haines, I.A. Galkin, J.L. Green, R.F. Benson, S.F. Fung, W.W.L. Taylor, P.H. Reiff, D.L. Gallagher, J.-L. Bougeret, R. Manning, D.L. Carpenter, S.A. Boardsen, First results from the Radio Plasma Imager on IMAGE. Geophys. Res. Lett. **28**(6), 1167–1170 (2001)
B.W. Reinisch, M.B. Moldwin, R.E. Denton, D.L. Gallagher, H. Matsui, V. Pierrard, J. Tu, Augmented empirical models of plasmaspheric density and electric field using IMAGE and CLUSTER data. Space Sci. Rev. (2009, this issue)
K. Rönnmark, Genereration of magnetospheric radiation by decay of Bernstein waves. Geophys. Res. Lett. **12**(10), 639–642 (1985)
C.T. Russell, R.E. Holzer, E.J. Smith, OGO 3 observations of ELF noise in the magnetosphere, 1. Spatial extent and frequency of occurrence. J. Geophys. Res. **74**(3), 755–777 (1969)
C.T. Russell, R.E. Holzer, E.J. Smith, OGO 3 observations of ELF noise in the magnetosphere, 2. The nature of the equatorial noise. J. Geophys. Res. **75**(4), 755–768 (1970)
J.C. Samson, The spectral matrix, eigenvalues, and principal components in the analysis of multichannel geophysical data. Ann. Geophys. **1**(3), 115–119 (1983)
B.R. Sandel, A.L. Broadfoot, C.C. Curtis, R.A. King, T.C. Stone, R.H. Hill, J. Chen, O.H.W. Siegmund, R. Raffanti, D.D. Allred, R.S. Turley, D.L. Gallagher, The Extreme Ultraviolet imager investigation for the IMAGE mission. Space Sci. Rev. **91**(1–2), 197–242 (2000)
O. Santolík, D.A. Gurnett, Transverse dimensions of chorus in the source region. Geophys. Res. Lett. **30**(2), 1031 (2003)
O. Santolík, M. Parrot, L.R.O. Storey, J.S. Pickett, D.A. Gurnett, Propagation analysis of plasmaspheric hiss using Polar PWI measurements. Geophys. Res. Lett. **28**(6), 1127–1130 (2001)
O. Santolík, J.S. Pickett, D.A. Gurnett, M. Maksimovic, N. Cornilleau-Wehrlin, Spatiotemporal variability and propagation of equatorial noise observed by Cluster. J. Geophys. Res. **107**(A12), 1495 (2002)
O. Santolík, D.A. Gurnett, J.S. Pickett, M. Parrot, N. Cornilleau-Wehrlin, Spatio-temporal structure of storm-time chorus. J. Geophys. Res. **108**(A7), 1278 (2003)

O. Santolík, D.A. Gurnett, J.S. Pickett, Multipoint investigation of the source region of storm-time chorus. Ann. Geophys. **22**(7), 2555–2563 (2004a)
O. Santolík, D.A. Gurnett, J.S. Pickett, M. Parrot, N. Cornilleau-Wehrlin, A microscopic and nanoscopic view of storm-time chorus on 31 March 2001. Geophys. Res. Lett. **31**, L02801 (2004b)
O. Santolík, F. Němec, K. Gereová, E. Macúšová, Y. de Conchy, N. Cornilleau-Wehrlin, Systematic analysis of equatorial noise below the lower hybrid frequency. Ann. Geophys. **22**(7), 2587–2595 (2004c)
O. Santolík, D.A. Gurnett, J.S. Pickett, M. Parrot, N. Cornilleau-Wehrlin, Central position of the source region of storm-time chorus. Planet. Space Sci. **53**(1–3), 299–305 (2005a)
O. Santolík, E. Macúšová, K.H. Yearby, N. Cornilleau-Wehrlin, H.S.C. Alleyne, Radial variation of whistler-mode chorus: first results from the STAFF/DWP instrument on board the Double Star TC-1 spacecraft. Ann. Geophys. **23**(8), 2937–2942 (2005b)
O. Santolík, J. Chum, M. Parrot, D.A. Gurnett, J.S. Pickett, N. Cornilleau-Wehrlin, Propagation of whistler mode chorus to low altitudes: Spacecraft observations of structured ELF hiss. J. Geophys. Res. **111**, A10208 (2006)
S.S. Sazhin, Improved quasilinear models of parallel whistler-mode instability. Planet. Space Sci. **37**(6), 633–647 (1989)
S.S. Sazhin, M. Hayakawa, Magnetospheric chorus emissions: A review. Planet. Space Sci. **40**(5), 681–697 (1992)
M. Schulz, Eigenfrequencies of geomagnetic field lines and implications for plasma-density modeling. J. Geophys. Res. **101**(A8), 17385–17397 (1996)
R.L. Smith, Propagation characteristics of whistlers trapped in field-aligned columns of enhanced ionization. J. Geophys. Res. **66**(11), 3699–3707 (1961)
V.S. Sonwalkar, Magnetospheric LF-, VLF-, and ELF-waves, in *Handbook of Atmospheric Electrodynamics*, ed. by H. Volland, vol. II (CRC, Boca Raton, 1995), pp. 407–462
V.S. Sonwalkar, U.S. Inan, Lightning as an embryonic source of VLF hiss. J. Geophys. Res. **94**(A6), 6986–6994 (1989)
V.S. Sonwalkar, D.L. Carpenter, T.F. Bell, M. Spasojević, U.S. Inan, J. Li, X. Chen, A. Venkatasubramanian, J. Harikumar, R.F. Benson, W.W.L. Taylor, B.W. Reinisch, Diagnostics of magnetospheric electron density and irregularities at altitudes <5000 km using whistler and Z mode echoes from radio sounding on the IMAGE satellite. J. Geophys. Res. **109**, A11212 (2004)
V.S. Sonwalkar, D.L. Carpenter, A. Reddy, B.W. Reinisch, Magnetospherically reflected (MR), specularly reflected (SR), and backscattered (BS) whistler mode (WM) echoes observed on the IMAGE satellite: Whistler-mode sounding of electron density, ion composition (H^+, He^+, O^+), and density irregularities along the geomagnetic field line. J. Geophys. Res. (2009, submitted)
D.J. Southwood, Some features of field line resonances in the magnetosphere. Planet. Space Sci. **22**(3), 483–491 (1974)
L.R.O. Storey, An investigation of whistling atmospherics. Phil. Trans. R. Soc. (Lond.) **246A**, 113–141 (1953)
L.R.O. Storey, F. Lefeuvre, M. Parrot, L. Cairó, R.R. Anderson, Initial survey of the wave distribution functions for plasmaspheric hiss observed by ISEE 1. J. Geophys. Res. **96**(A11), 19469–19489 (1991)
D. Summers, B. Ni, N.P. Meredith, R.B. Horne, R.M. Thorne, M.B. Moldwin, R.R. Anderson, Electron scattering by whistler-mode ELF hiss in plasmaspheric plumes. J. Geophys. Res. **113**, A04219 (2008)
K. Takahashi, R.L. McPherron, Harmonic structure of Pc 3-4 pulsations. J. Geophys. Res. **87**(A3), 1504–1516 (1982)
T. Tamao, The structure of three-dimensional hydromagnetic waves in a uniform cold plasma. J. Geomagn. Geoelectr. **16**(1), 89–114 (1964)
R.M. Thorne, E.J. Smith, R.K. Burton, R.E. Holzer, Plasmaspheric hiss. J. Geophys. Res. **78**(10), 1581–1596 (1973)
R.M. Thorne, R.B. Horne, N.P. Meredith, Comment on "On the origin of whistler mode radiation in the plasmasphere" by Green et al. J. Geophys. Res. **111**, A09210 (2006)
V.Y. Trakhtengerts, A generation mechanism for chorus emission. Ann. Geophys. **17**(1), 95–100 (1999)
V.Y. Trakhtengerts, A.G. Demekhov, E.E. Titova, B.V. Kozelov, O. Santolik, D. Gurnett, M. Parrot, Interpretation of Cluster data on chorus emissions using the backward wave oscillator model. Phys. Plasma **11**(4), 1345–1351 (2004)
V.A. Troitskaya, A.V. Gul'Elmi, Diagnostics of the parameters of the magnetosphere and of the interplanetary space by means of micropulsations, in *Low-Frequency Waves and Irregularities in the Ionosphere*, ed. by N. D'Angelo. Astrophysics and Space Science Library, vol. 14 (1969), pp. 120–136
B.T. Tsurutani, E.J. Smith, R.M. Thorne, Electromagnetic hiss and relativistic electron losses in the inner zone. J. Geophys. Res. **80**(4), 600–607 (1975)
C.L. Waters, F.W. Menk, B.J. Fraser, The resonance structure of low latitude Pc3 geomagnetic pulsations. Geophys. Res. Lett. **18**(12), 2293–2296 (1991)

J.M. Watts, An observation of audio-frequency electromagnetic noise during a period of solar disturbance. J. Geophys. Res. **62**(2), 199–206 (1957)
D.C. Webb, The analysis of non stationary data using complex demodulation. Ann. Telecommunic. **34**, 131–137 (1979)
D.C. Webb, L.J. Lanzerotti, C.G. Park, A comparison of ULF and VLF measurements of magnetospheric cold plasma densities. J. Geophys. Res. **82**(32), 5063–5072 (1977)
K. Yumoto, Generation and propagation mechanisms of low-latitude magnetic pulsations–A review. J. Geophys. **60**, 79–105 (1986)